Title
Studies of Energy Transfer and Ligand Binding at the Surface of Indium Phosphide Quantum Dots

Author
Swabeck, Joseph Kennard

Publication Date
2019

Peer reviewed|Thesis/dissertation

Studies of Energy Transfer and Ligand Binding at the Surface of Indium Phosphide Quantum Dots

by

Joseph K Swabeck

A dissertation submitted in partial satisfaction of the

requirements for the degree of

Doctor of Philosophy

in

Chemistry

in the

Graduate Division

of the

University of California, Berkeley

Committee in charge:

Professor A. Paul Alivisatos, Chair
Professor Steve Leone
Professor Naomi Ginsberg
Professor Eli Yablanovitch

Spring 2019

Studies of Energy Transfer and Ligand Binding at the Surface of Indium Phosphide Quantum Dots

Abstract

Studies of Energy Transfer and Ligand Binding at the Surface of Indium Phosphide Quantum Dots

by

Joseph K Swabeck

Doctor of Philosophy in Chemistry

University of California, Berkeley

Professor A. Paul Alivisatos, Chair

Semiconducting quantum dots hold a great deal of promise in a variety of light-based applications like displays and bioimaging due to their bright and relatively narrow emissions. For each of these applications, an understanding of the surface of the quantum dots is important to maximize their efficiency, as the surface is home to most of the trap states in a quantum dot. One can either make use of these states as intermediates for energy transfer, or remove them to maximize the quantum dot's native emission. This dissertation will investigate both the coupling of a luminescent species to the surface of InP quantum dots, as well as investigate ligand-based passivations of the surface of InP quantum dots.

Chapter 1 of this dissertation gives an overview of the variety of materials that have been made into quantum dots, along with some of their applications. The coupling of quantum dots to emissive dopants is discussed, along with two passivation strategies that have been studied in nanoparticles: the growth of a passivating shell material around the emissive core and the use of ligands bound to the surface of the quantum dot to passivate trap states.

Chapter 2 details the coupling of InP quantum dots to emissive Yb^{3+} or Nd^{3+} contained in a YF_3 shell around the quantum dot, which are finally passivated with a LuF_3 or YF_3 shell to reduce non-radiative quenching. This geometry allows for the broad absorbance of the quantum dot core to be coupled to the narrow emission from the Yb^{3+} f-f transition at $\sim$976 nm. This work utilizes a wide variety of electron microscopy and x-ray characterization methods to investigate the structure of this novel geometry. Optical characterizations were used to show that excitation of the quantum dot core led to a transfer to an intermediate trap state before transfer to the emissive rare earth ion. Though the total system quantum efficiency was only around 0.5%, this work introduces a novel method of creating extremely narrow emissions from quantum dot based systems.

Chapter 3 details initial investigations on the thermodynamics of ligand interactions with the surface of InP quantum dots. Isothermal titration calorimetry was used to investigate the heats of reactions of a variety of organic ligands with InP quantum dots, while quantitative nuclear magnetic resonance spectroscopy was used to investigate the extent of ligand binding

to the surface of the quantum dots. It was found that carboxylate ligands, which are the most commonly used ligand in InP quantum dot synthesis, are not necessarily fully passivating the surface, but amine ligands strongly bind to the quantum dots and passivate more of the surface than the carboxylates do.

To my wife and parents

For your love and unending support.

Contents

List of Figures

List of Tables

Acknowledgments

Thank you to my family, especially my wife Crystal, for all of your support over the years. Your unflinching love and willingness to be excited about my esoteric research made my graduate career so much more bearable. I would also like to thank all my friends in the group, the College, and beyond for helping me enjoy my life outside of lab. The fun I had with you all certainly helped to keep me sane.

I would like to thank the numerous people I have had the chance to work with over the years on a wide variety of facinating projects. To Noah Bronstein for his help in learning the finicky art of nanoparticle synthesis and his numerous lab pro tips. To Stefan Fischer for helping me find the lanthanide ions that have made up the bulk of my graduate work. To the beamline scientists of end stations 10.3.2 and 12.2.2 for teaching me about the wonderful world of synchrotron experiments and late nights, and to Matthew Koc for keeping those late nights interesting. To the imaging staff of the Molecular Foundry for the opportunity to explore the wonderful world of electron microscopy. Finally, to all of the people I got to work with on such a variety of interesting projects from high energy physics detectors to how best to inflate a chicken lung. Your projects have made my graduate experience as rich as it was, and I thank you for that.

Finally, thank you to my advisor, Paul Alivisatos, for the wealth of opportunities that have been given to me from working in his group. The numerous collaborations and opportunities to work outside of the D-level would not have been possible without his advice and belief in the gift economy. That idea will stay with me moving forward, and I hope to be able to implement it as well in my own professional life as he has in his. I am also thankful for the ability to have forged my own path and to pursue what I found interesting. I feel it has made me a better scientist, and allowed me to really learn how to create new knowledge.

Chapter 1

Introduction

1.1 Semiconducting Quantum Dots and Their Applications

Semiconductor quantum dots (QDs) are nanomaterials that have a variety of properties that vary significantly from their bulk semiconductor counterparts, including their bandgap energies,[1] plasmonics,[2,3] phase diagram,[4–6] melting point,[7,8] and their solubility in a variety of different solvents.[9–12] The optical property changes are mostly caused by the quantum confinement effect,[1,13] where the size of the QD is smaller than the radius of an exciton in the bulk material, the Bohr exciton radius, causing the exciton to remain bound and experience a similar effect to a particle in a box of the size of the QD. As such, the absorption of a QD will be blue shifted from the bulk absorption, due to the increased energy of the interacting exciton, and the size of the QD (or the size of the box in the particle in a box model) will directly dictate where that absorption energy will be. QDs also have a relatively narrow emission spectrum stemming from the single lowest energy transition they possess, as there is essentially an atomic-like energy of excitation and emission.[14] Additionally, the relatively large surface of a QD, as discussed below, can induce additional changes as compared to bulk materials, and it is likely responsible for the structural property differences between QDs and their bulk counterparts.

These novel properties have caused QDs to be widely studied, and a large variety of different semiconductors have been made on the nanoscale, including group II-VI,[15–18] III-V,[19–21] IV-VI,[22–24] Si,[25,26] and ABX_3 perovskites,[27] among many others. The variety of semiconductors used, along with the ability to tune the bandgap via size, allows quantum dots to have absorption onsets and photoluminescent emissions throughout the visible and near infrared (NIR) regions of light. This flexibility has been exploited in a wide range of applications, including displays,[28–30] solid state lighting,[31] LEDs,[31–34] bioimaging labels,[11,35] solar cells,[36,37] and additive manufacturing inks.[38,39]

One application of QDs that has gained interest as an alternative solar energy conversion technology is the luminescent solar concentrator (LSC). The LSC utilizes a sheet waveguide

doped with luminescent species to absorb sunlight and concentrate it down onto a small solar photovotaic, such as a silicon cell.[40,41] Light coming from the sun or scattered off of buildings or clouds is absorbed by the luminophore in the waveguide and reemitted out at a longer wavelength (i.e. blue light is absorbed and red light is emitted). The light is then, mostly, captured in totally internally reflected modes of the waveguide before reaching the solar cell on the side. Initially proposed at a time when silicon photovoltaics were prohibitively expensive to make on a large scale, the luminescent concentrator offers a number of benefits in the age of inexpensive traditional solar. Luminescent concentrators are insensitive to the amount of scattered light, as the angle of incidence does not matter for the luminophore absorption. This is in contrast with other concentrator photovoltaics, where solar tracking is required to maintain perfectly normal solar incidence. LSCs can also reach higher concentration factors than traditional lenses, as the enhalpy cost paid by downshifting the light can outweigh the entropy cost of concentrating it.[42] Additionally, more expensive solar materials can be used to improve the efficiency, as the majority of the LSC's area is made up of a relatively low cost luminophore sheet rather than the expensive semiconductor solar cells.

The luminophore for an LSC must meet a few requirements.[43] The first is that the photoluminescent quantum yield (PLQY) of the luminophore must be very high, ideally greater than 99%. There must also be a large Stokes shift between the absorbed and emitted energy of the photons to pay the aforementioned entropy cost. Lastly, in recent embodiments of the LSC, photonic mirrors have been used to increase light trapping efficiencies, so the bandwidth of the luminophore's emission must be as narrow as possible due to mirror design constraints. Quantum dots, and especially doped QDs, offer a nearly ideal luminophore for this application.

1.2 Coupling Quantum Dots to Light Emitting Dopants

Using QDs as the hosts for an optically active dopant stems from the desire to combine the broad absorption profile of the QDs with the well characterized emission of the dopant. This type of structure is desirable for a variety of reasons. One of the most recognizable properties of QDs is that the bandgap emission is tunable with size, but this is not always a desired effect. In cases where a large Stokes shift is desired (such as luminescent concentrators), it is better to shift the absorption profile to the blue while keeping the emission at lower energies. This is not strictly possible in traditional QD architectures, though efforts have been made to simulate this kind of shift by growing a larger bandgap material around the emissive core. Another benefit of this kind of system is that it creates an emission that is insensitive to the local environment of the QD. Properties such as the electronegativity of the ligand on the surface of the dot or the solvent environment can shift the emission of the QD,[44] but having a known emission is important for predictability of design. Since the dopants emit from atomic transitions, effects that are beyond the lattice of the QD do not affect them as

much. Despite these advantages, these kinds of systems typically have lower PLQY values than their QD only counterparts, so their applications tend to be somewhat limited.

Early work in the field focused on doping Mn^{2+} into II-VI QDs, such as CdS, ZnS, or CdSe.[45–48] These systems have shown fairly high PLQY values of up to 58%,[49] showing that the transfer of energy from the QD to the dopant is quite efficient and fairly complete, as evidenced by the quenching of the band edge emission. A variety of different geometries have been explored, from doping dots of the various materials to even well controlled doping of atomic clusters.[50] In each of these systems, the energy from the QD is transferred to the Mn^{2+} dopant, exciting the spin forbidden $^4T_1$ - $^6A_1$ transition. This then emits in a well characterized peak at ∼600 nm, giving a somewhat broad (due to vibronic and inhomogenious broadening effects)[51] orange emission.

Another type of doping has been the use Cu^+ as a non-emissive, trap inducing dopant.[52,53] This method follows a different logic from what was described above, as instead of taking advantage of energetic transitions within the dopant ion, the dopant is used to create an emissive trap state within the bandgap of the QD. This method does not result in the well characterized emissions of the Mn doped QDs, but it does allow higher bandgap materials such as CdS to have an emission in the red-NIR region of the spectrum. This is attractive due to the difficulty in producing good NIR materials, so being able to use well explored visible materials in the NIR could provide a facile route to the NIR emissions needed by dual junction iterations of the aforementioned luminescent concentrators. The disadvantages of this method are that the breadth of the trap state emission makes them a poor fit for the current design of luminescent concentrator, as the dielectric mirrors would have to block a large amount of light and lower the efficiency of the second cell. Additionally, since the system focuses on utilizing a defect-based emission, passivation and control of the emission become difficult.

A final doping scheme is to utilize emissive rare earth ions as the dopant. This method differs from the above Mn^{2+} based system because it uses f-block elements, whose emissive states are shielded by the $5s$ valence orbitals of the atoms. This results in a system where the transitions are relatively insensitive to the local environment around the atoms, meaning the broadening that is seen in Mn^{2+} emissions is not observed in f-block systems. This results in very narrow emission linewidths (∼10 meV for the rare earths compared to ∼230 meV for Mn^{2+}), which are typically more desirable. The same electronic structure that gives narrow linewidths also makes these ions have an extremely narrow absorption band, making sensitization all the more important. Doping schemes using rare earths are discussed in much greater detail in section 2.1, but are mentioned here for completeness.

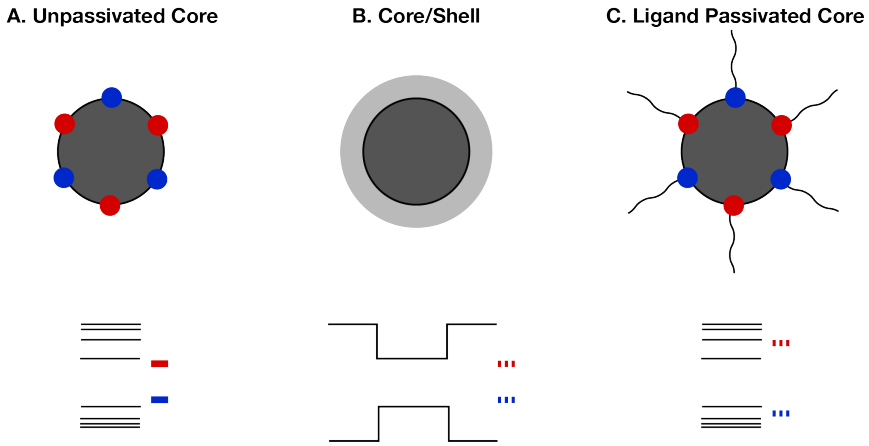

Figure 1.1: Cartoon schematic of quantum dot passivation schemes. (A) An underpassivated core QD with both electron and hole traps on/near the surface. Their presence in the bandgap of the QD could result in non-band-to-band relaxations, including non-radiative phonon processes or radiative trap state emissions. (B) Schematic of a core/shell QD. The shell has passivated the surface traps and provides a physical barrier against solution based quenching pathways. (C) Ligand based passivation. The ligands bind to the underpassivated surface sites and drive the states up in energy till they become resonant with the bands of the QD.

1.3 Surface Effects and Considerations of Colloidal Quantum Dots

Through the study of creating luminophores for LSC applications, it became readily apparent that the surface of the QDs made a very large impact on the overall luminescence properties of the QDs and the efficiency of the LSC as a whole. Quantum dots are typically thought of as perfect materials, due to the small size of the nanoparticle allowing most defects to be annealed out of the crystal,[54,55] but the surface of the QD is far from this vision. A variety of different trap states can exist at the surface of a QD, stemming from undercoordinated atoms,[56,57] imperfectly attached degradation induced species (such as oxides),[58] or the nearby proximity of solution phase quenchers. This idea is shown in cartoon form in Figure 1.1 A, the unpassivated QD core. Since the vast majority of applications of QDs rely on having a high luminescence efficiency, it is important to control the surface electronic energy levels and how they interact with the confined QD states in order to have the most efficient system possible.

Because the surface area of a sphere scales as r^2, compared to the r^3 scaling of the volume, the surface area as a ratio of the total volume increases significantly as materials are shrunk down to quantum confined regimes. As such, the surface begins to play a more significant role in the electronic structure of the material.[57] Micron sized grains in traditional semiconductors are relatively unlikely to have large numbers of defects within the grain as defects tend to form on the surface and there is relatively little surface area compared to

the volume of the bulk grain. Even still, with the low number of defects that are formed, the defects play a decisive role in the properties of bulk materials. At the nanoscale, these species can have an even more significant effect on the overall properties of the QD, since they make up a much larger proportion of the material. Small differences between the ideal and synthesized lattices, such as point defects or dangling bonds, will create energetic states that are deleterious to the optical performance of QDs. Additionally, the surface of the QD is in contact with the environment around it, meaning that external quenchers like ligand vibrations[59] or energy accepting species[60] in solution can non-radiatively remove energy from the QD. Due to the importance of the surface, additional study of what happens there was motivated to determine what the best surface passivations are for these nanomaterials. A variety of different methods have been attempted to help improve the luminescence of QDs, including shell growth and small molecule/ligand passivation. These effects are also discussed in brief in section 3.1, but will be addressed here in depth.

Improving the Optical Properties of Quantum Dots *via* Inert Shell Growth

The concept of growing an epitaxial shell of wide bandgap material was one of the first passivation routes that was investigated, starting with QDs grown in a matrix of another material via molecular beam epitaxy.[61] Initial efforts in the colloidal QD literature focused on creating quantum dot quantum wells of a low bandgap material sandwiched between layers of a higher bandgap material, such as CdSe/HgSe/CdSe.[62] This gave way to methods that instead consisted of a core QD surrounded by a shell of a higher bandgap semiconductor, such as CdSe/ZnS[63] or CdSe/CdS.[64] In each of these methods the important feature was that coating the emissive, lower bandgap QD core in a wider bandgap material creates a barrier that keeps the exciton generated by light absorption at the center of the QD, as seen in Figure 1.1 B. Since the surface of the QD tends to have the highest density of nonradiative pathways, this architecture keeps the core excitation from relaxing through phonon processes. Additionally, since these systems use a material that can form a nearly perfect epitaxial interface with the core QD, the shell also functions as a surface passivant, removing traps by coordinating all of the surface atoms of the core.

The concept of shelling QDs to improve the observed optical properties has been extended beyond simply shelling a semiconductor with another semiconductor. Using other materials that can physically separate the excitation from the surrounding environment have been proposed, such as silica[10] or LnF_3,[65] but they do not seem to show the same level of passivation as epitaxially grown shells. Since these methods do not have ideal surface attachment, trap states produced by underpassivated surface atoms can persist, even after shelling, causing the resultant system to be of a much lower quality than systems where the shell material grows perfectly from the surface of the QD. The benefit of these methods is that one can use these types of core/shell structures in different environments than an epitaxially shelled system. For example, if the QDs are used as biological labels, presenting an inert silica shell

decreases the toxicity of the QDs and improves the stability, though the quantum yield will suffer from the proximity of quenching groups.

In indium phosphide (InP) QDs, a number of shelling materials have been considered to improve the optical properties of the QDs. For colloidal methods of shelling, the most popular have been to use ZnS or ZnSSe as the shell material.[66–68] These methods have reached PLQY values of over 90% in recent years, but a number of problems still remain. The lattice mismatch between the InP core and the Zn based shell is significant, around 8%, so the total size of shell that can be grown is limited. Additionally, the strain that is induced at the interface of the core and shell can have deleterious effects on the PLQY of the emission, possibly lowering the upper limit of efficiency that is achievable. Interestingly though, for InP QDs the use of post-synthetic ligand modification has not been extensively studied for improving the optical properties of the QDs.

Utilizing Ligands and Other Small Molecules to Improve Quantum Dot Luminescence

Ligands play an important role in the synthesis of colloidal nanoparticles, as they not only impart the nanoparticles with their colloidal stability, but they also control important properties such as the shape[16,69,70] and superlattice assembly of the particles.[71] One of the benefits of colloidal syntheses is that they allow for the post-synthetic exchange of the ligands on the surface of the nanoparticles. This has been used to impart a number of different effects on the QD, from dramatically increasing the solubility limit of QDs to nearly gram per milliliter levels,[72] to changing the type of solvent used for the QDs from organics to water,[11] to improving the PLQY of an unshelled QD to near unity by removing trap states from the QD band,[73,74] as seen in Figure 1.1 C. The number of different applications for ligand exchanges shows the importance of the QD surface, as well as the power of understanding the surface and its interaction with various ligands.

For InP QDs, the most commonly investigated ligand passivation scheme has been the utilization of fluoride ions to etch and passivate the surface of the QD.[44,75–77] These processes have been used because they remove surface traps created by underpassivated surface phosphorous atoms through a simple removal of those atoms without affecting the stability of the QDs. Because surface traps in InP are different for the different excited species (indium is an electron trap while phosphorous is a hole trap), there is difficulty in producing a treatment scheme that passivates the traps without reducing or oxidizing the ligand for the other species, thus making a new trap. The prevalence of fluoride based schemes comes from its ability to do exactly this.

An interesting point with the F^- passivation of InP by removing underpassivated phosphorous atoms is that it is a photochemical process, where light was shown to be integral to the improvement of the PLQY in F^- treated samples.[75] As such, photogenerated excited holes are likely to play a part in the passivation process, as the capture of the hole by a surface undercoordinated P atom allows for the passivation reaction to occur. Recent work has

also shown that lower concentrations of HF can instead passivate surface In atoms' dangling bonds. This creates an opportunity for new surface passivation schemes using F^- ions.[44]

Other organic ligands for the passivation of InP have not been extensively studied, though $ZnCl_2$ has been shown to improve the PLQY of InP QDs when added as a post-synthetic treatment in recent efforts within the Alivisatos group. This is thought to be due to the removal of the same hole traps on underpassivated P atoms by coordinating them with the Zn. This method holds a lot of promise, as it improves the PLQY of InP QDs in an easily scalable way, without the use of highly toxic reagents like HF. Additionally, the addition of $ZnCl_2$ would be much easier than full ZnS or ZnSe shell growth, as it can be done at relatively mild temperatures. This type of passivation deserves more study, as inorganic ligands have been largely overlooked for QD passivation.

The aim of this dissertation is to look at two ways of interacting with the surface of InP QDs. The first is to attempt to use the imperfect surface as an ideal location for luminescent dopants to extract energy from the QD to be emitted, while the second is to attempt to understand better the interactions of the surface to improve the passivation and thus the native light emission of the QD.

Chapter 2

Visible to Near-Infrared Downshifting *via* Lanthanide Decorated Indium Phosphide Quantum Dots

Adapted with permission from Swabeck, J.K.; Fischer, S.; Bronstein, N.D.; Alivisatos, A.P. "Broadband Sensitization of Lanthanide Emission with Indium Phosphide Quantum Dots for Visible to Near-Infrared Downshifting", *Journal of the American Chemical Society* **2018**, 140, 9120-9126.

2.1 Background

Most applications for luminescent species benefit from the luminophore having a combination of the most broad possible absorption coupled to the narrowest possible emission. This is especially true in dual junction luminescent concentrators, where the absorbed bandwidth of the luminophore is directly related to how much power will be downshifted for the solar cell to absorb but the breadth of the emission dictates how much light will be blocked from reaching the lower junction. As such, creating a luminophore with a narrow emission coupled to a broad absorption is of value to not only solar energy conversion, but a variety of fields where narrow emission, broad absorption, or both combined can improve efficiencies. One of the most narrowly emitting species available are trivalent lanthanide (Ln) ions, as discussed in section 1.2 and further discussed below.

Ln ions are used in a wide variety of optical applications due to their manifold of narrow, atomic emissions that span the visible and NIR. They have been used in energy conversion schemes,[78–80] bioimaging,[81,82] and other applications where a narrow emission linewidth is desirable.[83] Ln ions also exhibit very long (typically ms) photoluminescent lifetimes, allowing for interesting photophysical interactions such as up- and down-conversion to occur.[84] Along with these benefits come a variety of difficult challenges. The narrow linewidths of the emission come from the fact that the transitions within these atoms are atomic-like, meaning

that the energies that can be absorbed are nearly as narrow as the emissions themselves. This limits applications by decreasing the effective wavelength range of the absorption.[85] For example, solar energy conversion would not be a suitable application of these materials, as the narrow absorption profile means that relatively little sunlight would be downshifted or upconverted to useful NIR light. Additionally, the forbidden nature of the f-f transitions means that the absorption cross section of Ln ions is very small compared to that of QDs or dyes, necessitating large numbers of ions in order to have practical absorption values for a luminophore material, which can result in increasing amounts of lossy processes such as ion to ion cross relaxation or energy migration to non-radiative quenching centers.

A wide variety of methods have been used to try to overcome one of the largest of these limiting factors in Ln ions, the weak absorption, while maintaining the narrow line width. These methods include the use of sensitizing organic molecules, other Ln ions with larger absorption cross sections, and QDs. A summary of these methods can be found in Table 2.1. Organic dyes and complexes[86] have long been employed as sensitizing agents for Ln ions and, due to the level of study that has been given to these materials and the close proximity of the excitation on the organic to the emissive ion, PLQYs of 75% have been reported.[87] Though the absorption of the Ln ion is improved by adding these dyes, they still do not offer a fully broadband absorption profile or the level of passivation that is necessary for achieving very high (>95%) PLQYs due to the lack of a protective, passivating shell to separate the Ln ion from solution phase quenchers. Because of this, non-radiative quenching processes are very present and can have a large impact on the PLQY of the material.[88] In addition to the use of organic dyes, other lanthanide ions, such as cerium, have been used as high-energy sensitizers when coupled to emissive Ln species. These systems use more allowed high energy $4f$-$5d$ transitions to overcome the forbidden nature of the typically observed $4f$-$4f$ transitions. Though these are not as strong as s-p transitions, they are nevertheless much stronger than the normally observed f-f transitions. This increases the cross section of the absorption, and it can result in a much more efficient downshifting and downconversion process.[89] This method is limited to fairly high energy photons (>4.5 eV in fluoride hosts[90]), which limits the usefulness of this method in most applications.

QDs have a number of desirable properties as possible sensitizers for Ln ions. Since QDs are semiconductors, they have a strong and broadband absorption above their band gap. Additionally, the band gap of a QD is tunable by a variety of different methods, including its size, shape, composition, and shell material.[67,94] This allows for the selection of the ideal absorption profile for the desired application. Additionally, the tunability of the band gap allows for changing the energy offset between the QD and the Ln ion, allowing for the engineering of the transfer rate and a systematic study of the mechanism. Previous work on QD based Ln ion sensitization by the Meijerink group showed that it is indeed possible to couple the absorption of a QD to the emission of a Ln ion.[95] Their work showed that one could adsorb Yb^{3+} to the surface of a cadmium selenide QD, and that there was energy transfer from the QD to the $^2F_{5/2}$ state of the Yb^{3+} that resulted in an emission event in the NIR. This work also showed that the surface passivation of the system is key for maximizing PLQY and stability, though even with an overgrowth of a selenium shell around the adsorbed

Material	Broadband Absorption	Absorption Coefficient	PLQY	Stability	Emission Linewidth	Toxicity
$PbIn_2S_4$[91]	Yes (intrinsic band gap ~1.4 eV)	$\sim10^5$ / cm	~5%	Medium	~25 nm	High (Pb)
$CsPbCl_3$[92]	Limited to UV-Blue	$\sim10^5$ / cm	~170%	Very Low	~25 nm	High (Pb)
YbF_3[93]	No (Limited to the transition itself)	~22 / cm	~0%	Medium	~5 nm	Low (Insoluble)
Organic Dye-Yb Couple[87]	Limited to UV-Blue	$\sim10^3$ / cm	~75%	Medium	~50 nm	Unknown

Table 2.1: Comparison of Literature Ln Ion Sensitization Methods

Yb^{3+} the emission from the Ln was fairly weak and no PLQY value was reported. Other work from the Gamelin group showed stable Yb containing particles could be made via a cation exchange.[91] This work reported a PLQY of ~5%, though further improvements may be difficult, as a large passivation layer is typically necessary for optimum PLQY and shell growth on $PbIn_2S_4$ has not been deeply explored. Additional work, also from the Gamelin group, has shown the use of $CsPbCl_3$ as a host for Yb^{3+} ions that, when excited at high energies, results in a quantum-cutting effect that can produce PLQY values of over 170%.[92] These particles have very impressive luminescence properties, but the relative narrowness of the absorption (<400 nm), the stability of the perovskite host lattice, and concerns about the toxicity of lead will hinder their widespread use.

Coupling Ln ions to InP QDs

From the above discussion of various lanthanide hosts, it is clear that QDs have the highest concentration of desirable properties to sensitize Ln ions, but the current literature methods each lack something. The CdSe based system is too dim, while all QD based systems (including the bright $CsPbCl_3$) mentioned above have severe toxicity or stability issues. As such, a new method of sensitizing Ln ions with QDs was developed to address these concerns. A stable downshifting configuration that combines the broad absorption of an InP QD with the narrow emission of the Yb^{3+} made by coating the InP QD core in a shell of ytterbium-doped yttrium trifluoride ($Y_{1-x}Yb_xF_3$) and growing a final passivating shell of LnF_3, where Ln is Y or Lu. This core/shell/shell structure was found to undergo energy transfer when exciting the InP QD above its band edge to the Yb^{3+} $^2F_{5/2}$ state, where a sharp NIR emission at 976 nm was observed. The advantages of this geometry are that the main components, InP and various rare earth fluorides, are stable and exhibit a lower toxicity than cadmium and lead containing nanoparticles. The optical properties of Ln doped glasses have been well studied, and it has been shown that these materials are

capable of some of the highest reported quantum efficiencies.[96] They have also been shown to be easily grown as nanoparticles, and large passivating shells can be grown to improve their optical properties.[97]

2.2 Synthesis Overview

An overview of the synthesis of the previously described core/shell/shell nanoparticles is found in Figure 2.1. This scheme has been shown to work for both Yb and Nd as the emissive Ln ion, but the majority of the work presented in this chapter will focus on using Yb as the luminescent center due to the simplicity of its energy levels. Full synthetic details can be found in Appendix A, as well as a detailed discussion of the effects of oxidation on the InP cores and the ability to adhere Ln ions to their surface. This effect is so important that a brief discussion of this effect will follow here as well. It is important to note that the trace oxygen present in ultra-high-purity (UHP) argon typically used in Schlenk lines can have a large impact on the properties of InP QDs. Even using 99.9995% argon results in a significant amount of oxygen on the surface of the particle, and this oxide shell can improve the luminescence efficiency of unshelled nanocrystals by orders of magnitude, reaching around 3% PLQY for band edge emission from heavily oxidized particles. Additionally, in an earlier version of attempting to couple Ln ions with InP it was found that moving from standard purity argon (99.5%) to UHP argon (99.9995%) resulted in a marked decrease of the NIR luminescence from the Yb^{3+}, as well as no evidence for Yb-P bond formation via extended x-ray absorption fine structure (EXAFS). Further purifying the argon to sub part-per-billion levels of O_2 resulted in the total elimination of the NIR luminescence. This is likely due to the removal of the oxide leaving an In-rich facet that would not favor Yb binding. This suggests that the reactive oxygen contained in a standard Schlenk line results in an oxide covered InP surface, and that surface oxide is essential to adsorb Yb onto InP. Again, this is explained in more detail in Appendix A, but its importance necessitates its repetition. The inability of Yb to adhere to the non-oxidized crystals resulted in the Ln fluoride scheme rather than relying on surface adsorption. Due to the insensitivity of the Ln fluorides to the InP's surface oxidation, they have proven to be a more robust method of adhering Ln ions to QDs.

The full details of the synthesis can be found in Appendix A. Briefly, InP cores were synthesized according to literature procedures with minor changes,[20] besides the addition of sub part-per-billion argon to the Schlenk line. Cleaned InP QDs were then treated with tetrabutylammonium fluoride (TBAF) to passivate the surface, attempt to remove trace oxygen impurities from the surface of the particle by replacing it with fluoride, and to provide a fluoride rich layer for the rare earth ions to adhere to. The treatment of InP with fluoride ions has been investigated in the literature, and this process follows similar methods to that literature.[19,75] These treated QDs were then shelled using trifluoroacetate (TFA) rare earth salts, $Y(TFA)_3$ and $Yb(TFA)_3$ to create the optically active Ln ion layer. Finally, an inert shell was grown using $Y(TFA)_3$ or $Lu(TFA)_3$ to complete the synthesis and passivate

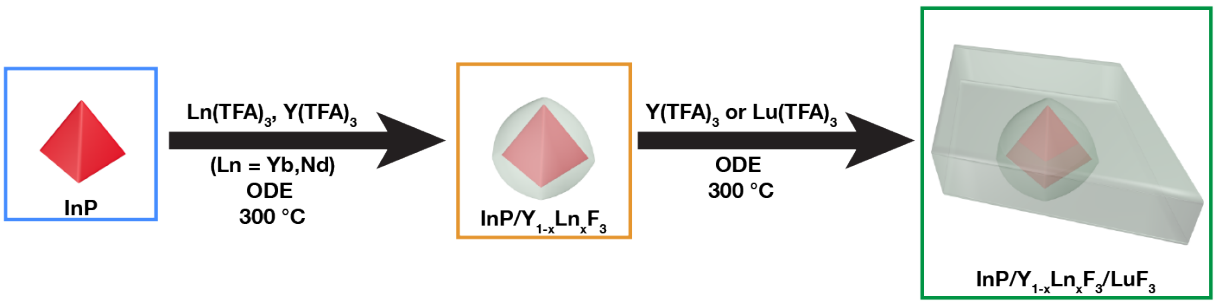

Figure 2.1: Overview of the synthesis of core/shell/shell nanoparticles. Corresponding TEM images are found in Figure 2.2

the optically active layer.

2.3 Electron Microscopy Characterization

Low Resolution Transmission Electron Microscopy

Low resolution TEM images of the core, core/shell, and core/shell/shell nanoparticles are found in Figure 2.2. The InP cores show a reasonable size dispersion throughout the sample, while the first shelling step appears to be quite inhomogeneous. This is likely due to some amount of nucleation of smaller particles of $Y_{1-x}Yb_xF_3$ in addition to the shelling of the InP QDs. This is unlikely to impact the optical properties of the completed core/shell/shell system, as any particle without an InP core would not absorb the visible light used in the experiments and would simply be a non-interacting additional species in solution. The final core/shell/shell particles are consistent in shape with established syntheses of LuF_3 found in the literature.[98] Additionally, it should be noted that a size selective precipitation was employed to remove smaller impurity nanoparticles and achieve the final product shown in Figure 2.2 C. If the reaction mixture is used there is some degree of inhomogeneity in the particles (as seen in Figure 2.5), though the size selected particles show a high degree of homogeneity, as seen in the low resolution TEM.

Scanning Transmission Electron Microscopy

Further electron microscopy was performed to confirm the core/shell/shell geometry of the final nanocrystals. Figure 2.3 A shows a high angle annular dark field scanning transmission electron microscopy (HAADF-STEM) image of the particles shown in Figure 2.2 C. Since HAADF-STEM has atomic number contrast, one expects the center of the nanocrystal to appear darker in correspondence with the lighter indium and yttrium that should be present there. The outside of the particle would then appear brighter, as the heavier lutetium that makes up the outermost shell would scatter more electrons than the light core.

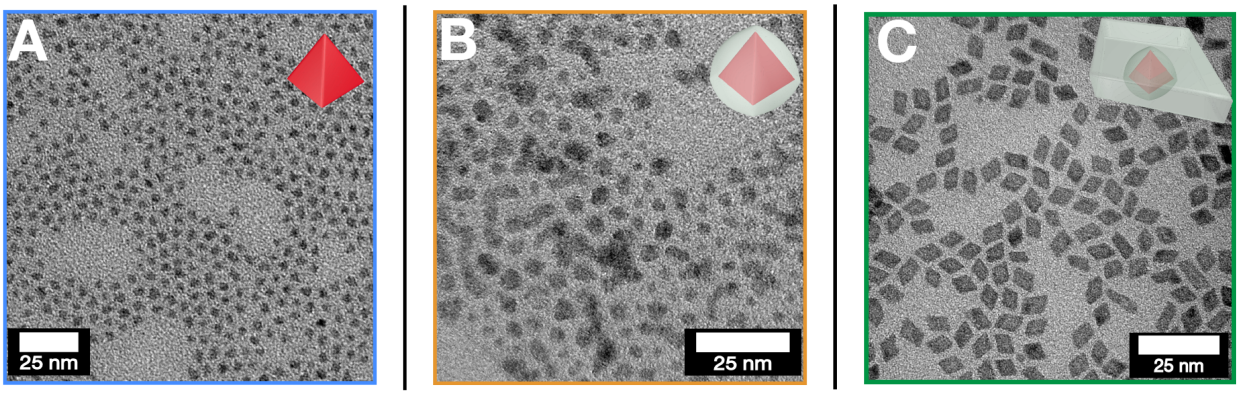

Figure 2.2: Low resolution TEM image of each step of the core/shell/shell synthesis. (A) TEM image of core InP QDs before any shelling steps or surface treatments occurred. (B) TEM image of InP/$Y_{1-x}Yb_xF_3$ core/shell nanocrystals. (C) TEM image of the completed InP/$Y_{1-x}Yb_xF_3$/LuF_3 core/shell/shell nanocrystals after a size selective precipitation was used to create a monodisperse sample.

The contrast difference can be quantified by radially integrating the contrast from the center of the nanoparticle to the edge and plotting this values against the distance. Figure 2.3 B shows the result of performing this process for 86 independent particles and averaging the results. The shaded region represents the standard deviation observed for the process.

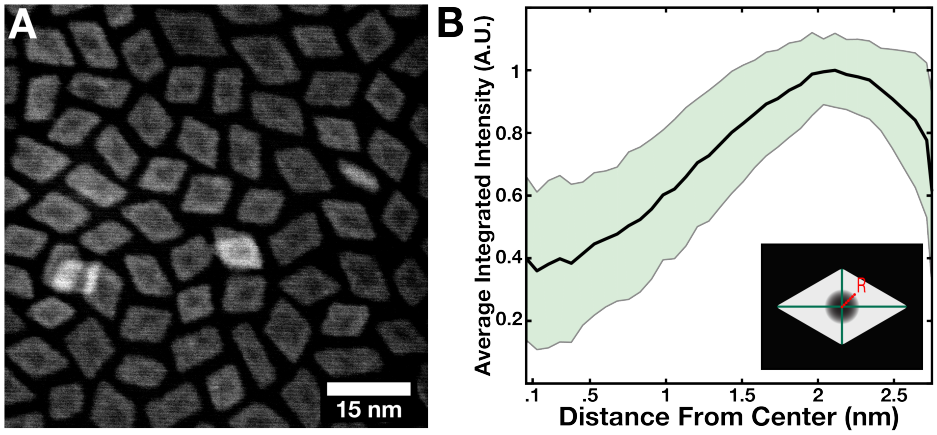

Figure 2.3: HAADF-STEM image and corresponding intensity integration. (A) HAADF-STEM image of the core/shell/shell nanocrystals. The contrast difference observed between the center and edge of the nanocrystal is due to the Z^2 contrast function of HAADF-STEM, where lighter elements appear darker in the image. (B) Radially integrated contrast values and standard deviation for 86 nanoparticles from images like that seen in A where lower contrast gives a lower integration value. The inset shows a cartoon of the process of finding the center of the particle and integrating out from it.

To produce Figure 2.3 B the following procedure was performed, and it is represented

schematically in Figure 2.4. In Image J, lines were drawn from the opposing corners of the nanocrystal to one another, and the intersection of those points was used as the center. The center point of each particle was saved into a list, where they were set as the center of a radial integration of the contrast value. To perform the radial integration, a circle is drawn around the central point, and the contrast value of the image along that surface is summed, which creates a value for the contrast intensity at that distance from the center. In Figure 2.4 this is shown with differently colored concentric rings where warmer colors are later circles. The plot in Figure 2.4 B shows an example of what the integrated contrast value would be at each point. One can see that in the left example nanocrystal by the third radial integration circle the contrast has maximized, so that circle would have a normalized value of 1. Since the contrast does not continue to increase beyond that circle, the final radial integration circle would also have a normalized contrast value of 1. This contrasts the right example, where the low contrast portion of the nanocrystal is not perfectly centered. In this case, the largest ring of the radial integration exceeds the size of the particle. Because of this, the integrated intensity of that ring would be lower than that of the one before it, since it is now summing the low contrast background into the integration which artificially lowers the value. Repeating this process many times creates a number of contrast curves, and from these an average and standard deviation can be extracted.

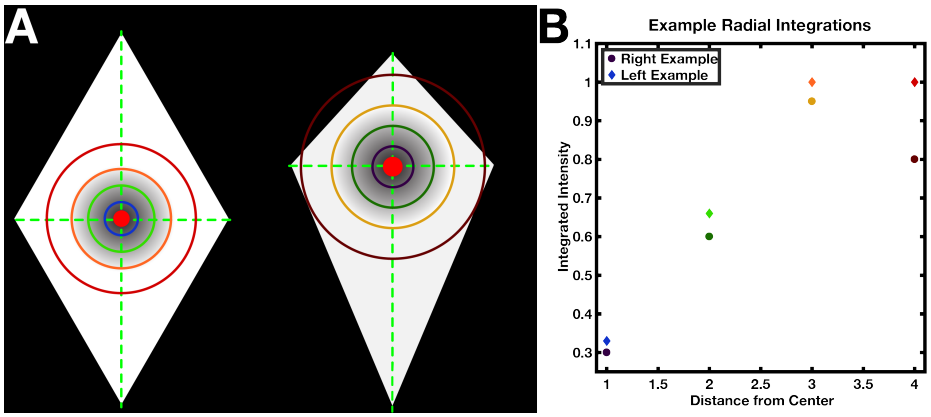

Figure 2.4: Example of the radial integration process for HAADF-STEM images. (A) Cartoon schematic of the contrast radial integration process. The green lines show how the 'center' of the particle was found, with the bright red dot showing the center. Example radial integration rings are shown originating from the center of the particle. The lines are then used in B. (B) Example radial integration plot using the example lines from A. The contrast value at each line is shown plotted against the distance from the center of the nanoparticle.

The integrated contrast values seen in Figure 2.3 B are in line with what would be expected from an In and Y core. The normative values for this were calculated via the following method. The thickness of the core/shell/shell nanoparticles was determined to be ~4 nm by looking at side stacked plates like those found in Figure 2.5, and was confirmed by Scherer analysis of the relevant x-ray diffraction (XRD) reflections. The InP cores were

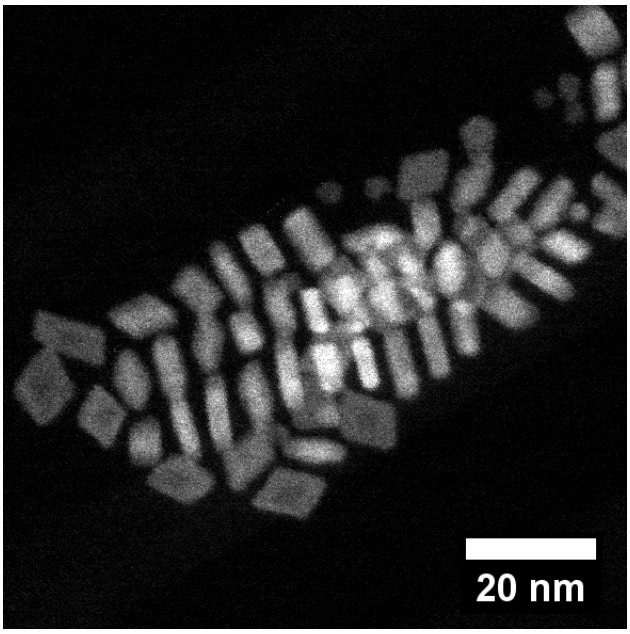

Figure 2.5: HAADF-STEM image showing the side view of the core/shell/shell nanoplates. This image shows the nanoplatelets to be ∼4 nm in height. Note that this sample did not have as rigorous of a size selective precipitation applied to it, resulting in the subpopulation of dots that are seen.

determined to be 3.7 nm in diameter by the position of the first exciton absorption energy. Using the d-spacing for both InP and LuF_3 (which was used due to its similarity to YbF_3, whose d-spacing was not available), we converted these width values into the number of unit cells of InP and YbF_3 present in the core of the particle (approximately 6.5 and 1, respectively). The number of unit cells was then multiplied by the atomic number of the dominant scattering species (In and Yb), and that number was then compared to a full 4 nm stack of LuF_3 unit cells (∼9 unit cells for the 4 nm of particle). The value that was determined for the core was then divided by the value for the shell, and the result gives the expected contrast ratio of 0.45. The below equations show this process.

$$Z_{\text{shell}} = 71$$

$$Z_{\text{core}} = \frac{6.5}{7.5} \times 49 + \frac{1}{7.5} \times 71$$

$$Contrast\ Ratio = \frac{Z_{core}^2 \times 7.5}{Z_{shell}^2 \times 9} = \frac{20228}{45369} = 0.45$$

The found value of 0.45 fits well within the error of Figure 2.3 B. As the integration moves away from the center of the particle, the LuF_3 shell becomes more dominant of a

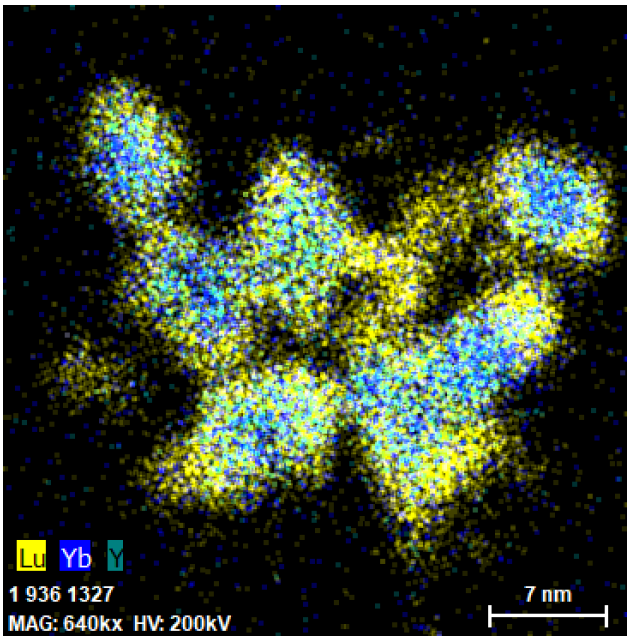

Figure 2.6: STEM-EDS image of core/shell/shell nanoparticles. The presence of Y and Yb in the core of the nanocrystal is confirmed, as is the Lu richness of the shell.

scatterer and the observed contrast goes to the full normalized value of 1 beyond the core of the nanocrystal. Due to the presence of a short axis, the integrated contrast decreases once the size of the integration circle gets larger than the short axis, as explained in Figure 2.4.

In addition to HAADF-STEM, additional confirmation of the core/shell/shell structure comes from STEM energy-dispersive x-ray spectroscopy (STEM-EDS). STEM-EDS allows for nanometer-scale elemental mapping of nanoparticles, which can show where various elements are localized within a nanoparticle. A representative STEM-EDS image is shown in Figure 2.6. In all EDS maps that were taken of the core/shell/shell nanocrystals, the In and P elemental signals were very difficult to detect. For indium, EDS maps localized to the nanocrystals, but the overall signal was too low to determine if it was centered in the core or in the shell. The P peak appeared on the shoulder of the much stronger Y peak, making it very difficult to deconvolute the P signal from that of Y. For the elements that were resolvable (Y, Yb, and Lu), Table 2.2 shows the elemental percentages from ∼15 particles.

Element	Core Percentage	Shell Percentage
Lu	0.25	0.38
Yb	0.35	0.32
Y	0.40	0.30

Table 2.2: Rare earth position distributions as determined by STEM-EDS.

High Resolution Transmission Electron Microscopy Characterization

Further confirmation of the core/shell geometry of the particles was given by the high-resolution TEM (HRTEM) images of the core/shell/shell particles. In the image shown in Figure 2.7, two different lattices are shown to be overlapping in the center of one particle. The lattices were analyzed using a Fourier filtering method. To do this, the initial image was converted to Fourier space via the FFT function of Gatan Digital Micrograph. Since the FFT shows two lattice domains (which appear as bright dots in the FFT of different distances from the center), a mask can be applied to the FFT, keeping the areas shown in blue and green in Figure 2.8. Inverting the masked FFT of those regions allows for the decomposition of the image into its constituent lattices.

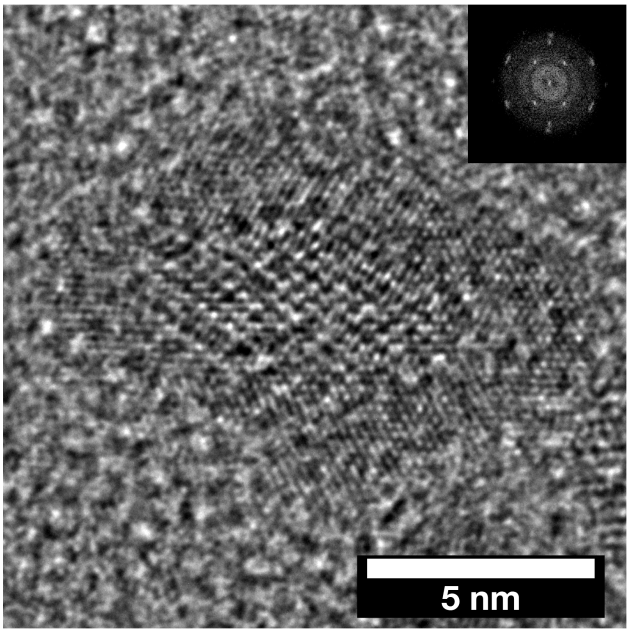

Figure 2.7: HRTEM image of a core/shell/shell nanocrystal. This image shows the lattice spacings of both the core and the shell of the nanocrystal overlapped on each other. The inset FFT also shows the clear signature of two in dependant lattices being present in the image.

In Figure 2.8 B, the core of the nanocrystal that came from the green region of the FFT is clearly seen. It is showing the [110] plane of InP, and it confirms that InP is at the core of the core/shell/shell system. Looking instead at the blue region of the FFT, the [001] lattice of LuF_3 is seen with its expected lattice spacing of 0.31 nm, observed in previous reports of these orthorhombic LuF_3 compressed from its initial parallelogram.[98] The lattice spacings of the $Y_{1-x}Yb_xF_3$ shell were likely not observed due to their similarity to the [001] plane of LuF_3.

Observing the alignment of the core and shell along the imaging axis of the TEM was rare. It was only seen in a few particles, but in each of them the InP [110] was consistently

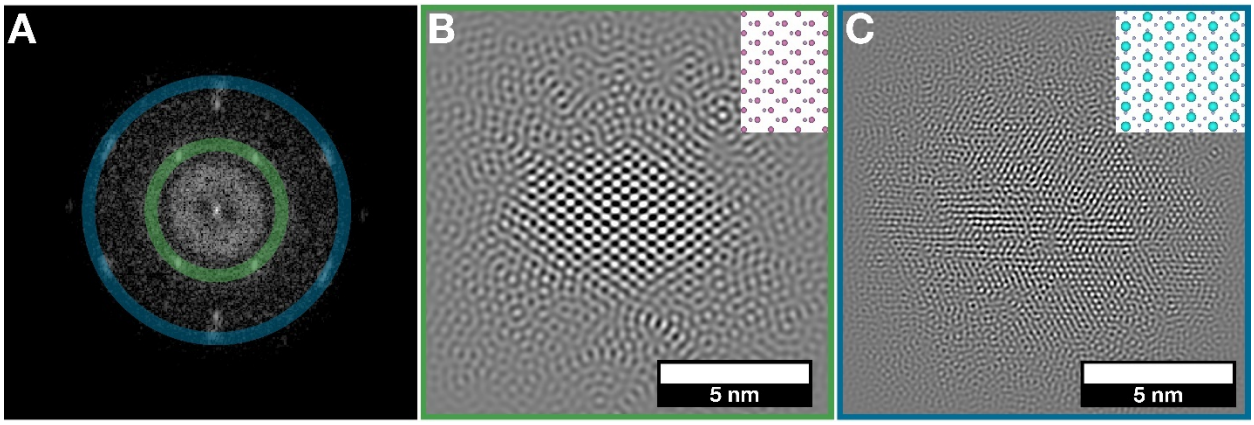

Figure 2.8: Fourier Filtering of a HRTEM Image. (A) The FFT of the initial image, showing the two independent lattice spacings. (B) and (C) Color coded inverse FFT's taken from the regions in A. The insets correspond to the atomic lattices of InP and LuF_3 respectively.

~30 offset from the LuF_3 [001]. Since there were very few particles observed this way, no conclusion can be drawn from the orientation angles, but studying this type of observation could provide insight into how these two different materials grow onto each other.

2.4 X-Ray Characterization

X-Ray Diffraction

X-ray diffraction was used to investigate the structure of the core/shell/shell nanoparticles, as seen in Figure 2.9. This technique confirms the phases of material that are present in the nanocrystal. The core InP shows heavy broadening, as the particles are very small. Once the first shell is grown, the XRD shows that there appears to be some preferential growth of the $Y_{1-x}Yb_xF_3$ shell. Since the shell is mostly yttrium, the reference reflections do not align with the observed reflections. The final shell shows that the lateral dimensions of the plate are quite large, as the reflections are quite narrow, though the other reflections related to the height of the platelet are broadened to the point of being unobservable. It is important to note that the InP reflections are present in each sample, and do not appear to be changing in size. This is important for the HAADF-STEM analysis discussed earlier in section 2.3, as it relies on the knowing the size of the InP core.

Extended X-Ray Absorption Fine Structure

Knowing the geometry of the core/shell/shell nanoparticles, the precise local environment around the optically active Yb^{3+} ions was investigated. In earlier versions of trying to attach Yb to the surface of InP it was found that Yb ions would not adhere directly to the In rich surface of InP and needed a surface oxide in order to adhere. Because of this, it was

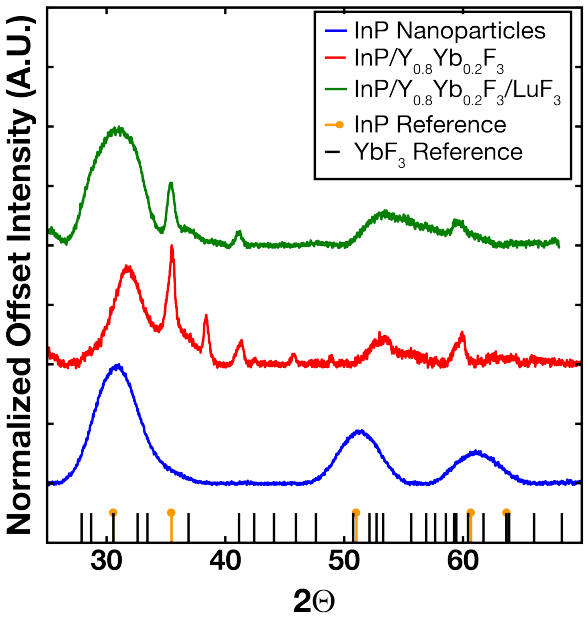

Figure 2.9: X-ray diffraction patterns of core, core/shell, and core/shell/shell nanoparticles. The core InP nanoparticles are shown in blue, core/shell in red, and core/shell/shell in green. The references are to cubic InP (PDF number 01-073-1983) and orthorhombic YbF_3 (PDF number 01-071-1161). The reference for LuF_3 was unavailable, so the YbF_3 shows roughly where the peaks should be found. Note that the LuF_3 reflections that correspond to the lateral dimensions of the nanoplatelets are sharp, while the ones corresponding to the height of the plate are broadened due to Scherrer broadening.

necessary to investigate the local structure around the Yb ions to see if an oxide was being formed, and how important it was to the structure of the nanoparticle. Extended X-Ray Absorption Fine Structure (EXAFS) is a technique that allows for the sensitive probing of the precise fine structure around an element, so it was used to see if the Yb was fully encased into the expected inert fluoride matrix. In addition to EXAFS, x-ray absorption near-edge spectroscopy (XANES) was taken to ensure that the Yb ions were in the expected, optically active, +3 oxidation state. It should be noted that for these measurements, since they rely on core level x-ray induced transitions, care must be taken in ensuring that all elements in the sample have no high energy transitions near the transition of interest. For example, Lu was not able to be used as the final shelling material for EXAFS samples, as its L_{III} transition at 9244 eV would interfere with Yb EXAFS. Another example is that the sample must have no Zn or Zn contamination, as its K edge transition at 9659 eV also interferes with the Yb EXAFS. As such, the samples used for these measurements were synthesized in the same way as those used for TEM and optical measurements, but the elements in the particle were selected to avoid any energy line contamination issues.

Observing the Yb^{3+} L_{III} edge XANES from InP/YbF_3 core/shell nanoparticles in Fig-

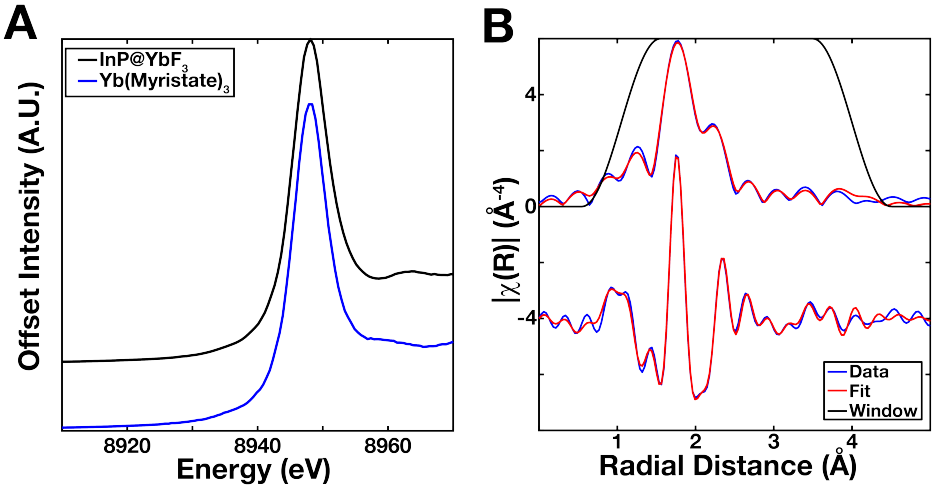

Figure 2.10: XANES and EXAFS spectra of the Yb L_{III} edge of core/shell/shell nanoparticles. (A) XANES comparison of the Yb found in InP/YbF_3 nanoparticles with the $Yb(Myristate)_3$ reference. The white line value is 8947 eV. Note that the difference in the EXAFS region is readily apparent between these two materials. (B) EXAFS data, fit, and window for $InP/YbF_3/YF_3$ core/shell/shell nanoparticles. The fits shown is to YbF_3

ure 2.10 A, one can see that the Yb is in fact in the expected 3+ oxidation state using a white line absorption energy value of 8947 eV. This is unsurprising, as the Yb was put into the system in a 3+ oxidation state, it is fairly stable in that oxidation state, and no strong reducing agents were added. It is still important that the Yb be in this oxidation state, as the 3+ state has the desired sharp NIR optical transition. It is also worth noting that even in the unprocessed EXAFS region, a clear difference can be seen between the Yb in the core/shell nanoparticles and the $Yb(Myristate)_3$ standard that is coordinated by oxygen atoms. Extracting the radial distribution function of the EXAFS gives the curves shown in Figure 2.10 B, which are found to be in good agreement with the YbF_3 crystal structure (PDF number 01-071-1161). This structure was found to be in far better agreement with the observed data than any other Yb based crystal structure that was used, including Yb_2O_3 or YbOF, and the fit of YbOF is shown below in Figure 2.11. Identical numbers of parameters were used in the two fits as not to bias the results. The parameters that were used were selected to provide the best fit of the data. The difference between the two fits is subtle, but Table 2.3 shows that the fluoride fit is much better than the oxy-fluoride fit, as evidenced by the much lower R-factor and the reduced χ^2, in addition to the presence of non-physical ΔR values in the YbOF fit seen in the detail of Table 2.4. This confirms that the Yb in the sample is in an optically active oxidation state and are contained within the desired inert fluoride matrix.

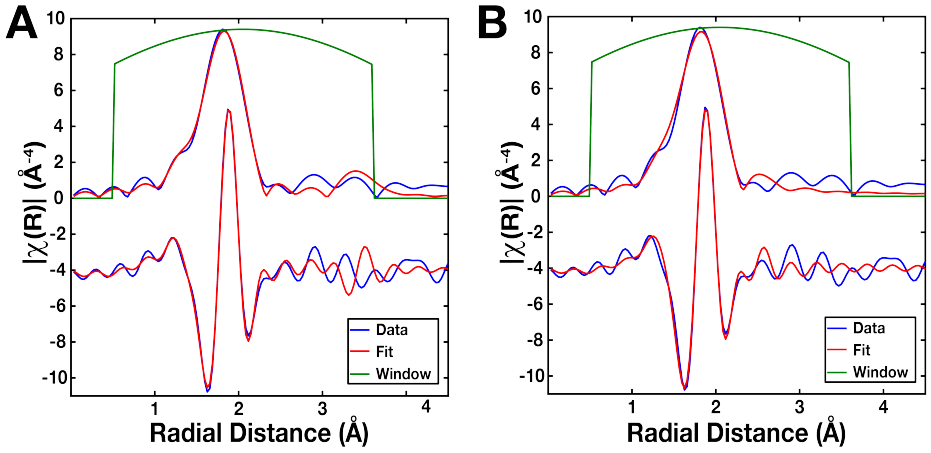

Figure 2.11: Comparison of EXAFS fits. (A) The fit of YbF_3 versus the fit of (B) YbOF.

Sample	YbF_3	YbOF
Independent Points	10.56	10.56
Number of Variables	7	7
χ^2	2549.16	5273.80
Reduced χ^2	716.34	1481.99
R-Factor	0.0122	0.0245
k-range (Δk)	2 - 10 (1)	2 - 10 (1)
R-range (ΔR)	1 - 3.1 (1)	1 - 3.1 (1)
Window Type	Kaiser-Bessel	Kaiser-Bessel

Table 2.3: Relevant data for the EXAFS fits in Figure 2.11.

Material	Path	N	$S_0{}^2$	s^2	E_0	ΔR	R_{eff}	R
YbF_3	$F_{2.1}$	2	1.129	0.0023	0.653	0.0341	2.2341	2.2682
	$F_{1.1}$	6	1.129	0.0145	0.653	-0.0584	2.2737	2.2153
	$F_{1.4}$	2	1.129	0	0.653	0.3299	3.5269	3.8568
	$F_{2.1}$-$F_{1.1}$	6	1.129	0.0084	0.653	-0.0121	3.5291	3.5170
YbOF	$O_{1.1}$	2	1.26	0	-0.579	0.0631	2.1920	2.2551
	$O_{1.3}$	2	1.26	0	-0.579	-0.1209	2.2469	2.1260
	$F_{1.1}$	1	1.26	0.0073	-0.579	0.0618	2.253	2.8715
	$F_{1.2}$	2	1.26	0	-0.579	-0.057	2.3516	2.2946

Table 2.4: Detailed parameters of the EXAFS fits in Figure 2.11.

2.5 Optical Characterization

Absorption and Photoluminescence

The first optical property that was investigated was the steady state absorbance of the various steps of the core/shell/shell synthesis. In Figure 2.12, the absorbance of the treated and native InP QDs is compared. The absorbance that is seen is very indicative of relatively monodisperse InP cores, and sizing the cores via the position of the first exciton gives a size of ∼3.7 nm. As expected, when the QDs are treated with the fluoride source, tetrabutylammonium fluoride (TBAF), the first excitonic peak shifts blue due to the small etching effect of this treatment. Since these QDs are strongly quantum confined,[99] small changes in the size of the QD will result in large changes in the position of the first exciton peak. There is also some amount of broadening in the absorbance, likely due to minor differences in the amount of etching coupled with the aforementioned strong quantum confinement. In the photoluminescence (PL), there is an apparent small oxide trap state emission on the red tail of the band edge PL due to the incredibly rapid oxidation of InP upon removal from the glovebox. In both fluoride treated InP and InP/YF_3 no trap state emission is observed, as seen in Figure 2.13. The lack of trap state emissions in these samples, even though they were handled exclusively outside of the glovebox, is important, as will be shown later in the discussion of the core/shell/shell luminescence spectrum.

The absorption and PL of core/shell/shell nanoparticles is shown in Figure 2.14 A. The first thing to note is that the absorption of the core/shell/shell system is very indicative of the InP core QDs, showing that the initial InP particles have slightly etched and broadened in size distribution during the shelling process, as the absorption has shifted even further blue and broadened from its native shape. This is likely due to the fact that the shelling procedure involves multiple hours at 300 °C, which is plenty hot enough to activate Ostwald ripening in InP QDs. Nevertheless, the size of the cores based on the position of the first exciton peak (3.5 nm diameter) is in good agreement with what the size of the cores was determined to be via the TEM in Figure 2.2 B as well as the integrated HAADF-STEM contrast in Figure 2.3.

The PL spectrum of the core/shell/shell nanocrystals show three distinct peaks that correspond to the different emissive states within the crystals that are shown in Figure 2.14. The first peak centered at 549 nm is attributed to the InP band edge emission, consistent with other works using InP of this size.[20] The presence of the InP band edge PL shows that the energy transfer to the Yb^{3+} from the QD is not complete, as there is still some amount of excitation in the QD that can radiatively recombine. The broad peak centered at 728 nm corresponds to an interband trap state that is between the band edge of the InP and the Yb^{3+} $^2F_{5/2}$ state, a level that has been proposed, but not observed, in InP thin films that have been ion implanted with Yb^{3+}.[100] Finally, the sharp peak centered at 976 nm corresponds to the Yb^{3+} $^2F_{5/2}$ to $^2F_{7/2}$ transition. The inset of Figure 2.14 A shows an expanded view of the peak under higher power illumination (∼10 mW), where the increase in the flux results in grater definition of the peak shape. The characteristic shape of this peak

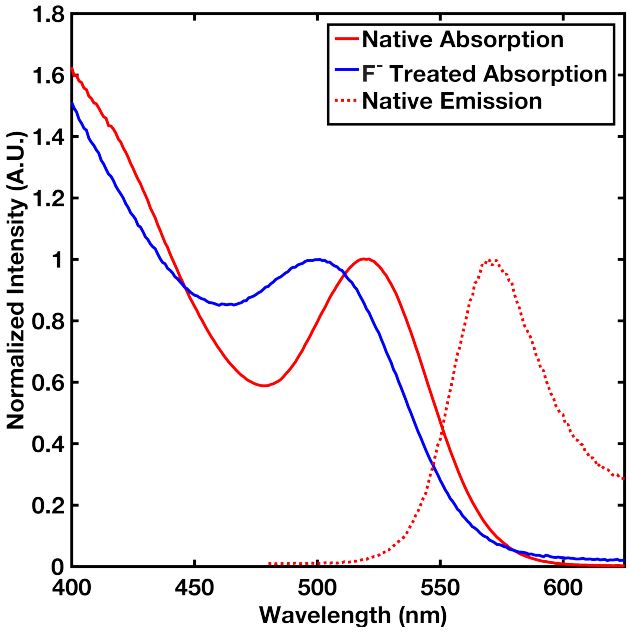

Figure 2.12: Comparison of the absorption and luminescence of native and fluoride treated InP. The PL of the native InP shows some small oxide trap state emission on the red end of the spectrum due to the rapid oxidation of the InP upon removal from the glove box to take these measurements. The PL of the fluoride treated InP QDs is found in Figure 2.13, and does not show the same oxidation.

clearly defines it as coming from Yb^{3+}, with the sharp feature at 976 nm being accompanied by a smaller, broader feature peaking at slightly longer wavelengths. Using a calibrated integrating sphere PLQY setup (the details of which are found in Appendix B) a PLQY of between 0.1% and 0.5%, depending on sample, was measured for the excitation of the core InP QDs (λ_{ex} = 440 nm) and emission from the 976 nm Yb based feature. The range of the PLQY seems to come from slight differences in the synthesis of the nanoparticles, with differing fluoride treatments having profound effects on the final system PLQY. In general, InP that has a higher PLQY after the fluoride treatment step tends to have a higher NIR PLQY from the Yb^{3+} in the final core/shell/shell system. This is likely due to higher visible PLQY after fluoride treatment corresponding to a more complete surface fluoridation, or possibly the more complete removal of oxygen from the InP surface. In either case, the effect could simply be a result of the more complete removal of non-radiative sites from the InP resulting in more energy being able to be shuttled to the Yb, but further study is necessary to determine the exact cause of this effect. Integrating the full spectrum (from ∼500 nm - ∼1000 nm) gives a PLQY of 3.5% for all emissive states in the nanoparticle.

It was mentioned earlier in this section that it is important that the treated and that the undoped shelled nanoparticles be free of any trap state emission. This is because the trap emission that is observed in the core/shell/shell nanoparticles appears to be not only induced by the presence of the Yb^{3+} in the optically active shell, but it is integral to the

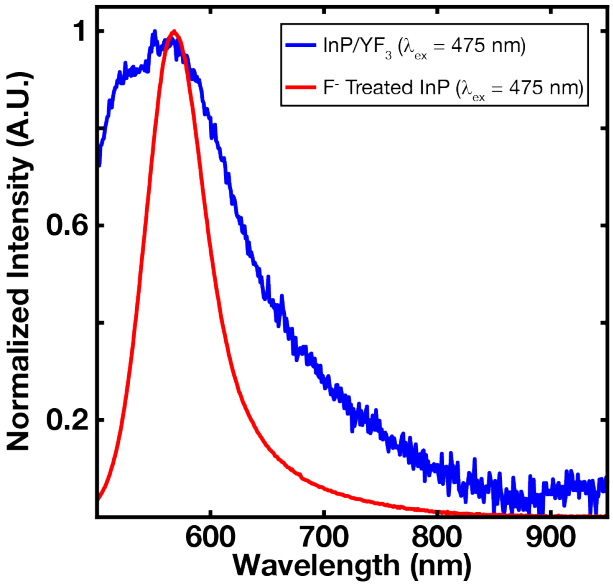

Figure 2.13: Photoluminescence spectra of treated and undoped nanoparticles. Fluoride treated QDs do not seem to show any trap state emission, as the surface has been better passivated by the F^- ions. Similarly, InP QDs with an undoped YF_3 shell grown around them do not show any trap emission either. This implies the trap observed in Figure 2.14 is likely due to the addition of the dopant.

energy transfer process. This can be seen in Figure 2.14 B, the photoluminescence excitation (PLE) scan of the core/shell/shell nanoparticles plotted against the absorbance of the same particles. The absorbance of the InP tracks very well with the PLE of the 976 nm emission above the band gap of the InP, but below the band edge there is a peak in the PLE that is not explained by the QD absorption. This gives insight into the path of the energy transfer from the InP band edge to the Yb^{3+} dopant, as this is evidence of the previously unobserved intermediate state. Since a PLE scan traces absorption events that lead to an emission, the presence of this sub-gap state shows that there is some state existing at that energy that can be excited to produce a Yb based emission. This state is not strongly absorbing, as the absorption of the core/shell/shell nanoparticles does not show it, but the fact that it appears in the PLE at all means that it is more efficient to excite the trap state directly than it is to excite the InP above the band gap. This is most likely due to the transfer step from the trap to the Yb^{3+} being much more efficient than the transfer of energy from the band edge to the trap. The relatively narrow appearance of the feature in the PLE could be due to the shallow nature of the Yb induced trap states that lead to an emission event. There are likely a large number of other trap states that do not result in energy transfer to the Yb, which would then explain the breadth of the trap state emission. Interestingly, when the PL spectrum is plotted in energy space, the breadth of the InP peak is of similar width to the breadth of the trap peak, suggesting that the breadth of the trap peak could be due instead

to the size dispersion of the InP. Determining exactly the reason for the trap's existence and why it seems that only some trap states lead to Yb emission would be an interesting point for further study.

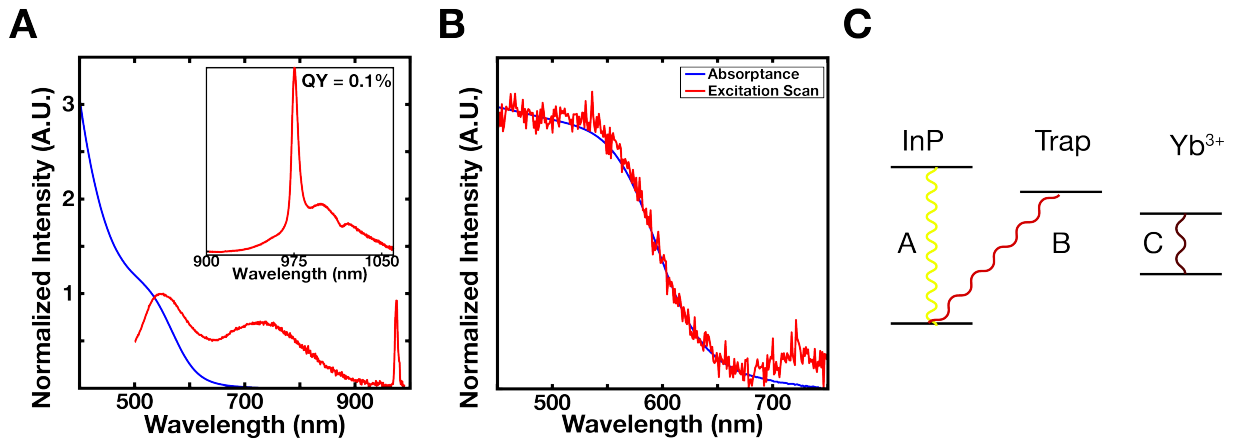

Figure 2.14: Absorption, photoluminescence, excitation scan, and band level cartoon of core/shell/shell nanoparticles. (A) The absorption and PL (λ_{ex} = 440 nm) of $InP/Y_{0.8}Yb_{0.2}F_3/LuF_3$ core/shell/shell nanoparticles. The inset shows a detail of the Yb^{3+} emission centered at 976 nm, agin under 440 nm excitation. (B) Absorbance (linear scale absorption, blue) vs the PLE of the 976 nm Yb^{3+} emission. Note the small increase in the PLE after 700 nm. (C) Cartoon of the band diagram for A. Transition a corresponds to the InP band edge emission, b to the broad trap state, and c to the NIR Yb^{3+} emission.

Taking all of these observations together, a more complete idea of the energetic states of the core/shell/shell system can be formed, as seen in Figure 2.14 C. The absorption of a photon into the InP core (transition A) results in a (relatively) high energy excitation that can transfer to the trap state. This trap state excitation can either recombine to the InP core (transition B) to produce the broad emission seen in the PL, or transfer further down to the Yb^{3+}. This excitation can then either non-radiatively quench or emit (transition C), which would result in the observed 976 nm emission. Based on the PLE, one could also excite the trap directly by pumping transition B, which would then proceed in the same way as an excitation formed by the transfer of energy from the InP core.

Time Resolved Photoluminescence

Further mechanistic insight into the luminescence process of the core/shell/shell nanoparticles can be derived from time resolved PL (TRPL) spectra. These measurements give information about how long it takes a state to radiatively recombine, and as a result can show the process of energy transfer within a system. In Figure 2.15, the band edge lifetimes of the InP cores of the different steps of the core/shell/shell reaction process. The shortening of the band edge lifetimes of the core/shell and core/shell/shell nanoparticles suggest that

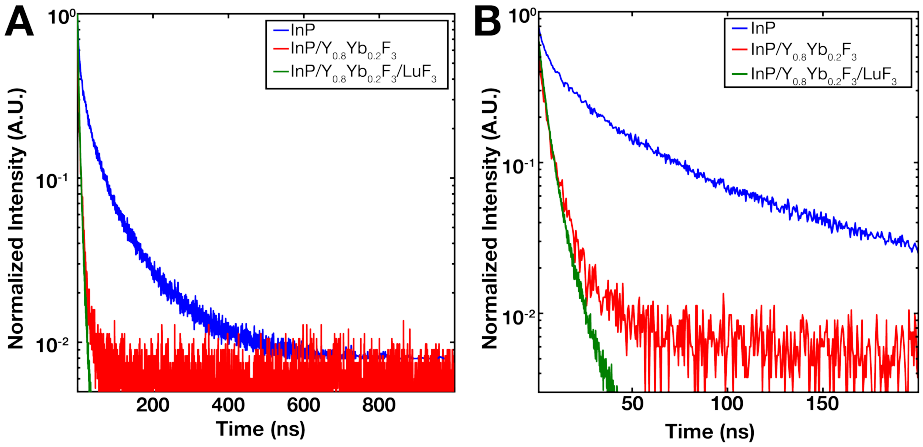

Figure 2.15: InP band edge emission lifetimes for each step of the core/shell/shell process. (A) InP band edge emission ($\lambda_{em} = 520$ nm) of native, core/shell, and core/shell/shell nanoparticles. (B) A zoomed in detail of the first 200 ns of A.

there are some additional processes that are occurring in those systems that result in a faster depopulation of the band edge. The exact identity of these processes is not obvious, and it could be that the energy transfer process is depopulating longer lived carriers, there could be other non-radiative processes, or some combination of the two. Additionally, the lifetimes of the core/shell and core/shell shell geometries have very similar values. This would suggest that the fact that the luminescence efficiency of the Yb transition is drastically improved in the core/shell/shell geometry is due to increased passivation of the Yb ions rather than any effect stemming from energy transfer from the QD. The core/shell TRPL is only collected over two decades because the PLQY of the band edge in that geometry is very low, and collecting this data to three or more decades would have taken an untenable amount of time.

In addition to the InP band edge lifetime, the Yb TRPL provides information about the energy transfer process that leads to a NIR emission. The lifetime of the 976nm emission of Yb under different excitation wavelengths is shown in Figure 2.16. The Yb luminescence decay can be well fit by a biexponential fit for all excitation wavelengths that were used. There are a number of reasons that this could be, but it is probably due to a number of competing rates being present stemming from the variety of local environments of the Yb ions (closer to the core vs closer to the surface, etc.). Due to this structural complexity, and not knowing where the biexponential nature of the fits are coming from, intensity weighted averages of the two lifetimes were used for analysis. The lifetimes that are observed for the Yb are 6.4 μs upon 760 nm excitation and 9.1 μs for 450 nm excitation. Since the lifetimes for the Yb^{3+} are much longer than those from the QD band edge, we can assume that the Yb NIR emission is insensitive to the upstream kinetics of energy transfer. This is to say, the observed lifetimes are not likely to have been caused by some sort or competing process of back transfer or slow transfer from the band edge or trap. The mechanism could be through a surface based Yb induced trap that would form as the result of the Yb binding to the

surface species of the QD, which would be consistent with the previous literature accounts of both thin film InP[100] and the recent work of doped perovskite QDs.[92] Alternatively, the mechanism could involve a trap state that is native to the InP, which has been previously seen in the literature,[19] that is co-opted into the energy flow from InP to Yb. In either case, the origin of the trap state does not impact the ability of the InP to transfer energy to the Yb in the first shell and, since the mechanism is extraordinarily difficult to exactly determine, we cannot exactly say what it is. In our system, the Yb is further from the lattice than in either the thin film or perovskite QD work, likely reducing the wave function overlap between the band edge of the InP and the Yb-related trap state. This would reduce the speed of the energy transfer dramatically. This is likely why we observe remaining band-edge PL after the full core/shell/shell overgrowth, and why the PLQY of the process of exciting the InP and emitting from the Yb remains low. The coupling of the core wave function to the Yb species could be improved in the future by selecting materials for their overlap, or creating nanostructures specifically designed for improving transfer efficiency. Once such method could be to grow an 'onion' structure, where alternating layers of InP and Yb doped material would spread the core wave function over the Yb and probably drastically improve the transfer efficiency.

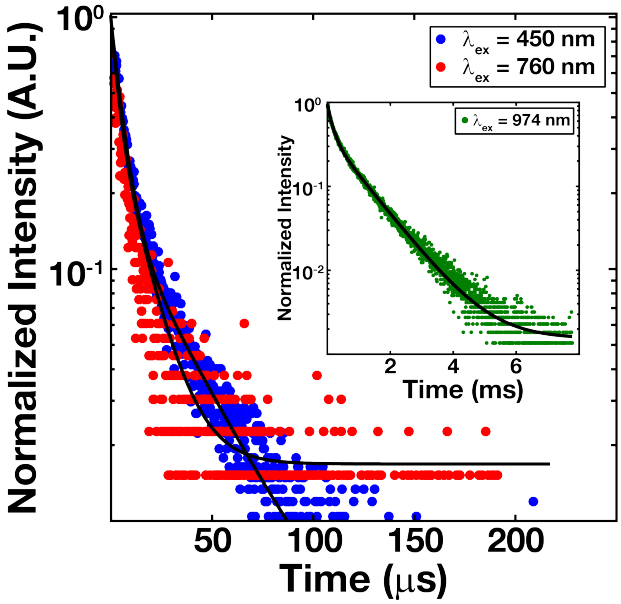

Figure 2.16: Lifetimes of the Yb^{3+} $^2F_{5/2}$ - $^2F_{7/2}$ NIR emission. The lifetimes here were taken using different excitation wavelengths: a 450 nm excitation of the InP core (blue), a 760 nm excitation of the trap state (red), and the direct 974 nm excitation of the Yb ions (green, inset). All lifetimes were fit to biexponential fits, which are plotted as solid lines.

The intrinsic lifetime of the Yb^{3+}, or the PL lifetime of the Yb^{3+} when it is directly excited with 974 nm light, is dramatically longer than the lifetimes when it was pumped

from the InP band edge or from the trap state at 495 μs, as seen in the inset of Figure 2.16. This is consistent with previous work in passivated lanthanide systems,[59] but it is not nearly as long as is seen in fully passivated Yb ions (1.9 ms in YF_3).[101] We assume that this is due to the plate morphology of the core/shell/shell nanocrystals, where the passivation that is achieved on the short axis of the material is not as good as what would be seen in a glass. This would allow for increased surface quenching to occur, which has been shown to dramatically decrease the lifetime of a Ln ion transition.[59] Additionally, there could be some diffusion of Yb ions into the final shell of the core/shell/shell system,[102] which would allow for ions to be closer to the quenching surface of the nanoparticle. Excited Yb closer to the core of the nanoparticle could have their energy migrate to the Yb ions in the final shell and non-radiatively recombine there, decreasing both the lifetime and the PLQY of the system.

Additional Optical Characterization

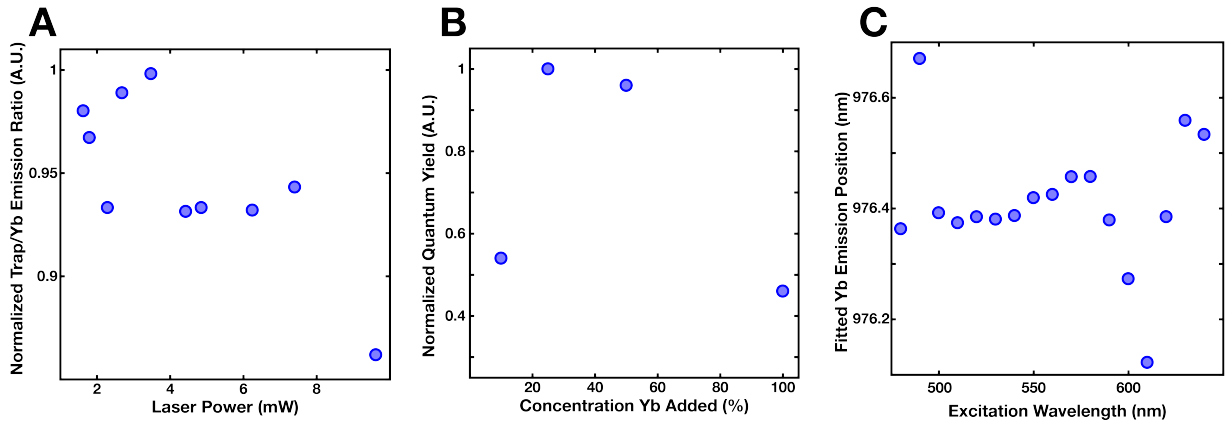

Figure 2.17: Power, concentration, and excitation laser wavelength effects on the luminescence of core/shell/shell nanoparticles. (A) Normalized ratio of the integrated intensity of the trap emission of core/shell/shell nanoparticles to the Yb NIR emission under various laser intensities. (B) Normalized PLQY of core/shell/shell nanoparticles at various Yb concentrations. (C) Peak wavelength position of the NIR Yb peak of core/shell/shell nanoparticles vs the excitation wavelength of the laser used to excite. Peak position was determined via Gaussian fitting the top half of the peak.

There is a well established literature on the effects of laser power and doping concentrations on Ln ion doped materials,[103] so it was important to ensure that the core/shell/shell particles were made at the appropriate doping level and that no laser induced artifacts were occurring. Plots of these tests are found in Figure 2.17. The first test that was carried out was to see if there was a strong excitation power dependence of the luminescence of the core/shell/shell nanoparticles. Varying the 440 nm excitation laser over a power range of $\sim$1 to $\sim$9 mW using a series of neutral density filters, the ratio of the integrated intensity

of the trap state emission was compared to the integrated intensity of the Yb emission. The values that were recorded in Figure 2.17 A show no clear trend, within error. This means that there does not appear to be a bottleneck in the energy transfer chain, so the particles are able to use as much power as is supplied. Changing the amount of $Yb(TFA)_3$ that was added to the $Y_{1-x}Yb_xF_3$ shell and recording the PLQY of the Yb 976 nm emission is shown in Figure 2.17. The results can be interpreted in three general regimes, namely a low, medium, and high concentration regime. At low concentrations there is not enough Yb present to have a significant interaction with the QD, so less energy is funneled into the Yb and down to the NIR emission. Another way to interpret the low PLQY is that since the lifetime of the Yb ions is very long, not having enough Yb present would mean that the few ions that were there could become saturated with excitations and not fully utilize all of the input light. In the medium concentration regime, there is enough Yb to interact will with the QD core and take in some of the excitations that are occurring, but not so many Yb ions (as there are in the high concentration regime) that there is an increased amount of non-radiative interactions (which likely involve energy migration to quenchers on the surface). The final control that was performed was to test the position of the Yb 976 nm peak when the excitation wavelength was varied. The precise peak was determined via a Gaussian fitting of the top half of the Yb peak. There does not appear to be a real correlation between the excitation wavelength and the peak position, again demonstrating the robust nature of the Yb emission. This also shows that there is no severe inhomogeneity of the Yb environments in the core/shell/shell system, where local field effects could shift the position of the peak.

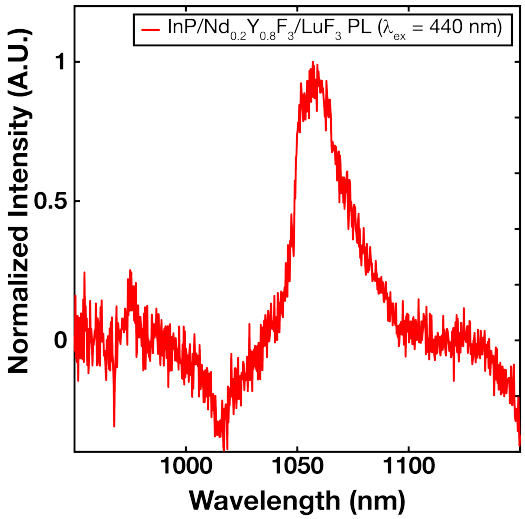

Figure 2.18: Photoluminescence spectrum of Nd doped core/shell/shell nanoparticles. PL of $InP/Y_{0.8}Nd_{0.2}F_3/LuF_3$ under 440 nm excitation showing the $^4F_{3/2}$ to $^4I_{11/2}$ transition. The dip in the PL just before the peak is due to a solvent absorption combined with the baselining process for the spectrum.

Expansion to Nd as an Optically Active Lanthanide

The final test of the robustness of the Ln ion doped core/shell/shell system was to use another Ln ion as the optically active species in the first shell. Neodymium was chosen for this purpose, as it has a wide variety of optical transitions and generally stronger transitions than Yb^{3+} does. The main emission line of Nd is found at 1064 nm, and it was found that using the same synthetic method as for Yb gave an emission at 1064 nm, as seen in Figure 2.18. The luminescence was very weak, probably due to the increased number of states leading to the possibility of cross relaxation and non-radiative transitions. The results, though low in PLQY, does demonstrates that the method described above can be fully extended to a variety of other Ln ions.

2.6 Conclusions

This work demonstrates the synthesis of core/shell/shell nanoparticles of InP/ $Y_{1-x}Ln_xF_3$/ ShF_3 where Ln is Yb or Nd and Sh is Lu or Y. These particles were shown to exist in the expected core/shell/shell geometry by a variety of electron microscopy and x-ray characterization techniques. Additional EXAFS measurements confirmed the good passivation of the optically active Ln ions in a fluoride matrix. Optically, the particles were shown to pass excitation from the band edge of InP through an optically active trap state to the Yb^{3+} $^2F_{5/2}$ transition, which led to an emission in the NIR at 976 nm with a PLQY of at least 0.1%. With further improvements to the optical efficiency of the system, it could provide a broad, tunably absorbing system with a sharp NIR emission that could be desirable in a variety of different applications. This embodiment of the core/shell/shell system also provides an insight into the mechanism of energy transfer from the delocalized state of a QD to the highly localized excitation of a Ln ion, which can help inform the design of other visible to NIR downshifters.

Future directions of this work would be broadly categorized in two main thrusts. The first would be to further improve the understanding of how the InP and LnF_3 interface. Due to the difficult in finding enough core/shell/shell particles properly aligned in TEM, there are a number of unanswered questions surrounding how these two different lattices can interact. More careful electron microscopy studies, such as larger area high resolution studies or strain field mapping could provide insights into how the lattices attach. Additionally, careful XRD simulation could also provide some of these answers. The second thrust would be to try to improve the optical efficiency of the NIR Ln ion emission. Previously mentioned novel particle geometries could help the overlap the the delocalized InP exciton with the very local Ln ions. In addition, further optimization of the shell growth to produce more isotropic final morphologies would likely decrease non-radiative depopulation of the excitations before they were able to transfer or emit. Investigating the trap state's importance and kinetics could also inform further development of this system. Both of these directions would be difficult, but the resultant luminophore could be of great importance to a wide set of fields.

Chapter 3

Ligand Interactions and Surface Thermodynamics of Indium Phosphide Quantum Dots

3.1 Background

Quantum dots have attracted increasing interest for their use as luminescent color centers in display[28–30] and imaging technologies[81,82,104] due to their spectral tunability,[27,94] color purity,[27,28,30] high PLQY[73,74,105] and solution processability.[106,107] To date, the best results in each of these categories has been achieved in cadmium based II-VI semiconductor materials. These QDs have achieved tunable emissions on the order of 80 meV wide with recently determined PLQY values of >99.5%.[105] These values make cadmium containing QDs ideal for use in consumer displays, but concerns over the toxicity of cadmium coupled with increasing regulation of the amount of cadmium that is permissible in consumer electronics has spurred the drive towards the development of cadmium free QDs. One possible alternative that is under investigation is the use of $CsPbX_3$ QDs, as they show highly tunable, narrow, and bright emissions across the entire visible spectrum.[27,108,109] These materials run into many of the same issues, though, as their low stability[110] coupled with the known toxic effects of lead place them into a similar category as the cadmium containing QDs. The current best alternative to these heavy metal containing QDs in indium phosphide (InP), which has similar intrinsic properties[111] to cadmium based II-VI QDs while exhibiting a significantly lower toxicity. Unfortunately, the state of the art of InP QDs lags significantly behind that of their cadmium containing counterparts. This is especially true of the optical properties (PLQY and linewidth) of InP QDs, where InP will have a PLQY orders of magnitude lower than CdSe while simultaneously having nearly double the linewidth. This can be seen in the data presented in Figure 3.1. In order to improve InP QDs to the same performance level as their cadmium containing counterparts, additional study, especially at the surface of the QD, must be done.

Much of the success of the cadmium containing QDs has come from the ability to remove deleterious surface effects.[112] As discussed in section 1.3, surface traps and quenchers can produce significant nonradiative processes, which then lower the overall quality of the optical properties that are observed. Mitigating those surface states is typically done by one of two methods, growing a shell around the QD[67] or employing a small molecule ligand as the passivant. Growing a shell of a wider bandgap material isolates the emissive core from nonradiative processes that occur at the surface. Additionally, the growth of a shell can funnel charge into the core, increasing the likelihood of an emissive event. Wide bandgap material shelling is very stable and has resulted in the brightest QDs to date,[105] but it comes at the cost of additional high temperature growth steps that make the control of the size distribution more difficult. Additionally, not every material has a wide bandgap couple that can be easily grown over it. This limits the applicability of this method to only materials that have a good epitaxy partner. A second, more general, route to improving the optical properties of a QD is to adjust the ligand that is on the surface of the QD. All colloidal QDs have a native shell of organic ligands as a result of the methods used to synthesize them that impart the QDs colloidal stability. By changing the composition of this ligand shell, one can improve the PLQY of the material by orders of magnitude. For example, it has been shown that the addition of amines to bare CdSe can improve the PLQY by over 100 times.[113] The method of using surface modification to improve optical properties is easily scalable and solution processable, but it has not yet been shown to be as effective at impacting the PLQY of QDs as shell growth has. To close this gap, additional investigations of the effect of surface ligands on QDs, especially InP QDs, must be performed.

Previous efforts on the surface passivation of InP QDs has largely focused on the use of halide ions as passivants, specifically using F^-.[75] The reactive fluoride ions etch the native

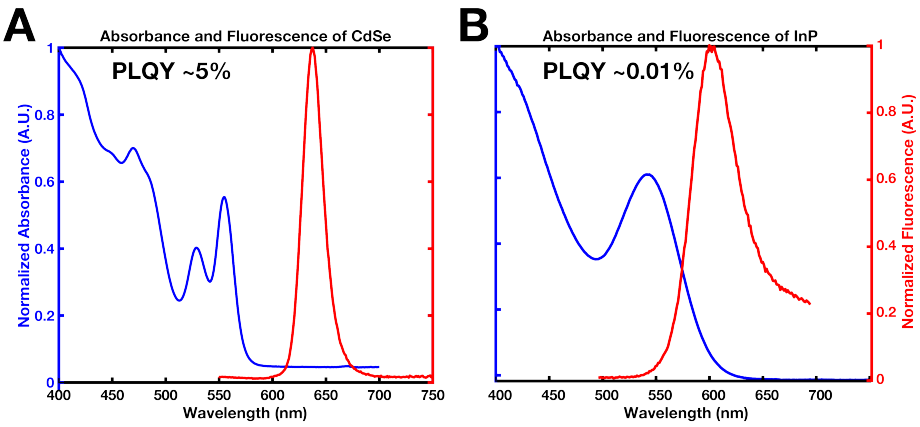

Figure 3.1: Comparison of the optical properties of CdSe and InP QDs. (A) The absorption and photoluminescence of CdSe quantum dots. (B) The absorption and photoluminescence of InP quantum dots. Note the extreme differences in linewidth and PLQY for the two as synthesized materials.

surface oxide of the InP QD and replace it with a fluoride passivated In rich [111] facet.[19] While this work has resulted in PLQY values in excess of 50%, it uses incredibly toxic reagents (such as HF) and does not typically allow for further passivating shells to be grown, if desired. An alternative to using reactive fluoride etching is to use organic/small molecule ligands. While these ligands have shown marked improvements in CdSe, as previously mentioned,[113] their use in InP systems has not been well explored. In this work, the thermodynamics of the interaction of ligands with the surface of InP QDs in an effort to better understand how to improve optical and colloidal properties through the introduction of tight binding and non-toxic ligands.

Methods for Investigating Ligand Surface Interactions

Due to the importance of QD ligands discussed above, a number of different techniques have been utilized to investigate how ligands interact with the QDs. The two that will be focused on in this chapter are isothermal titration calorimetry (ITC) and nuclear magnetic resonance spectroscopy (NMR).

ITC is a powerful technique for determining the heat generated or required for a chemical reaction to occur. It has found use primarily in the study of biological binding events,[114] but the simple requirements of the technique, that the reactants be suspended in the same solvent and that the reaction occur near room temperature, mean that it can be adapted to a variety of different reactions. This technique has even been used previously to thoroughly investigate the binding of catechol ligands to the surface of ZnO nanoparticles,[115] investigate the exchange of Ag ions into CdSe,[116] and to determine the sign of the enthalpy of other ligand reactions.[117–119]

The basic structure of an ITC is shown in Figure 3.2 A. A sample cell (filled with a solution of one part of the reaction) and reference cell (filled with solvent) are held at constant temperature, and a small amount of titrant (containing the second reactant) is added in. The instrument then records the change in the amount of heat that is needed to maintain that constant temperature (either positive or negative), which gives time resolved thermodynamic information as to the reaction, and can even show how many steps there are in the reaction, as shown in Figure 3.2 B and C. This information can then be interpreted to determine what kind of reaction is occurring, how many steps it has, and what its overall thermodynamics are. The ITC has a variety of benefits, including high signal to noise and resolution, relatively small sample sizes, low error, and the fact that the reaction can be recovered after the experiment and further quantified. One such further characterization is the use of NMR to determine the amount of bound ligand on the QDs.

NMR has been utilized extensively to study the binding of ligands to the surface of QDs due to the ease of determining the fraction of ligand that is bound to the QD, regardless of the presence of unbound ligand. This is due to the decrease in relaxation time of a bound molecule versus that of one free in solution substantially broadening the NMR peaks of the bound ligand, making it simple to determine how many ligands are on the surface of the QD. This has been used to investigate the exchange of various ligands on the surface of QDs,

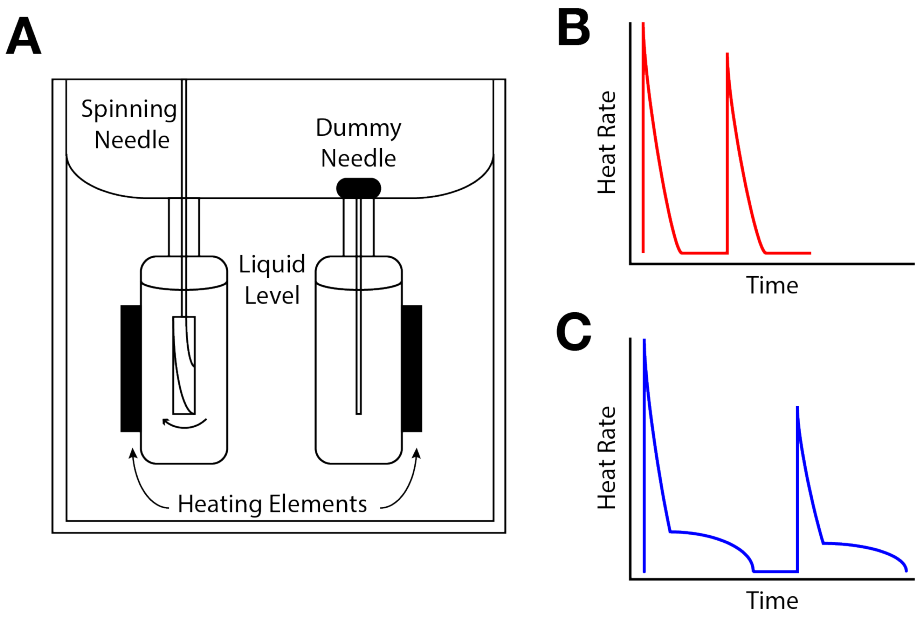

Figure 3.2: Cartoon Schematic of an ITC Apparatus with Example Signals. (A) Schematic of the working parts of an ITC. (B) Cartoon of expected data for a single event per injection. (C) Cartoon of more complex data where two events are occurring at different times.

including phosphonic acids on CdSe QDs[120] and tracking the addition of hydrophilic ligands on core/shell QDs.[121] In each of these cases, NMR was utilized for its ability to track bound ligands with reasonable accuracy in simple solutions.

The coupling of ITC and NMR provide a balanced quantification of the surface of a QD, as the ITC gives information about the heats of binding, a proxy for bond strength, but it does not give a clear picture of what exactly the ligands are doing to the QD (binding, etching, etc.). Conversely, NMR can give a detailed picture of the surface of the QDs, but it does not give any thermodynamic information. By combining these two techniques, and adding in optical characterization methods to track the surface traps of the QD, the surface of a QD can be explored in a way that has not been pursued in the literature. This chapter will detail the study of InP QDs via ITC and NMR.

3.2 Synthesis of InP Quantum Dots for Ligand Exchange Measurements

InP QDs used for this study were synthesized in a similar way to the procedure detailed in Appendix A, with one important difference. In the synthesis of InP for ligand characterization, 0.789 g of 1-octadecene was used as the solvent for the tris(trimethylsilyl) phosphine instead of .831 g trioctyl phosphine (TOP). This difference was due to the desire to have the

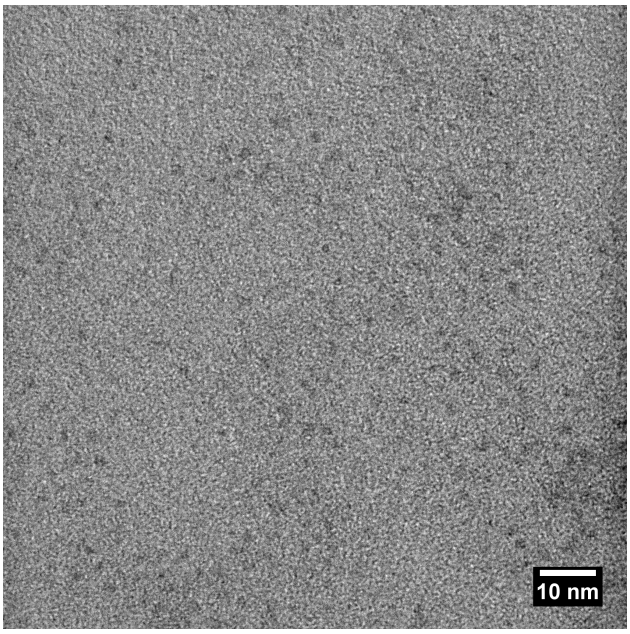

Figure 3.3: Representative TEM image for InP QDs used in thermodynamic studies. Note the difficulty in seeing the InP QDs, even though the image was taken on an ultrathin grid. This is due to their small size and light elements scattering the electrons poorly.

only coordinating species in the reaction be the myristate ligand (an unsaturated 14 carbon carboxylic acid). TOP has a lone pair on the phosphorous that can act as a L type (neutral donor) ligand to surface In species of the InP QDs. This would create a ligand shell with two species, which would severely complicate the ligand exchange studies by making there be two reactions instead of one. The result was that the QDs synthesized for the ligand exchange reactions were smaller ($\sim$3.2 nm) and more polydisperse than those made for the studies of Ln ion excitation coupling to QDs. A typical TEM image of the QDs made by this method is found in Figure 3.3, and their optical properties are seen in Figure 3.1 B.

The particles in this study were cleaned in the same way as in Appendix A, which is important for the study of their ligand properties. Cleaning with acetone and centrifugation does result in the removal of some of the native ligands from the surface of the QD. This certainly does impact the study of ligand interactions with the QD, but since this step is done before any of the other characterizations it should not induce any irreproducibilities into the study. Additionally, the QDs were synthesized under sub part-per-billion levels of O_2 and kept in an inert atmosphere glovebox until they were used for the experiments, which allowed for a controlled amount of surface oxidation and consistency between different runs on different samples of QDs.

3.3 Native Ligand Quantification of InP Quantum Dots

The initial ligand shell, the one that was present prior to exchange steps, was characterized using standard analytical NMR techniques. To do this, a known amount of a standard (mesitylene was used for this study) was added into a QD solution of known concentration. The integration of a mesitylene peak was compared to that of the ligand, and thus the ligand concentration was determined. Coupling this data with the concentration of QDs, as determined by the optical absorption, gave the number of ligands per QD in any given solution. The process of determining the exact amount of ligand is somewhat complicated by the fact that the entire carbon chain of the ligand is saturated, so there is no convenient handle for integration as there is in the unsaturated systems. The full process is detailed in section B.3. The full quantification of the native ligands gave a value of $\sim$8 ligands/nm^2, slightly above the literature value of 4 ligands/nm^2.[122] This discrepancy is likely due to the difficulty of determining the precise surface area of the QDs, due in part to the wide size distribution of InP QDs coupled with the difficulty of getting accurate TEM sizing curves. This difficulty is seen in Figure 3.3, where the small size and low contrast of the InP QDs result in poor imaging.

With the native ligands of the QD understood, two main thrusts of investigation were performed: the determination of the heats of ligand binding using an ITC and quantifying ligand surface coverage via NMR.

3.4 Thermodynamics of InP Ligands as Determined by Isothermal Titration Calorimetry

Details of the precise instrumentation used and a more detailed discussion of the data acquisition process is found in Appendix B. Four different ligands binding (or head) groups were investigated in their binding to the surface of InP QDs: amines, carboxylic acids, phosphines, and phosphonic acids. These head groups were chosen because they represent not only a variety of ligand binding types, but also because they are very commonly used in various QD syntheses. The first ligand binding curve is shown in Figure 3.4, corresponding to the addition of oleic acid to the InP QDs. When the baseline has been subtracted from the heat generated by the addition, the data shows a simple monotonicaly increasing binding curve that corresponds with a single binding event occurring. This event is likely the binding of oleic acid to the surface of the InP QD. Since the reaction is entirely exothermic, it means that the reaction that is occurring is composed of bond formation. The significance of this is that if the oleic acid was displacing native ligands there would be an endothermic portion of the data corresponding to the breaking of the indium-myristate bond. Using this interpretation, the addition of oleic acid to InP seems to simply add more carboxylic acid to the surface without displacing native ligand. This means that the surface of InP, or at least

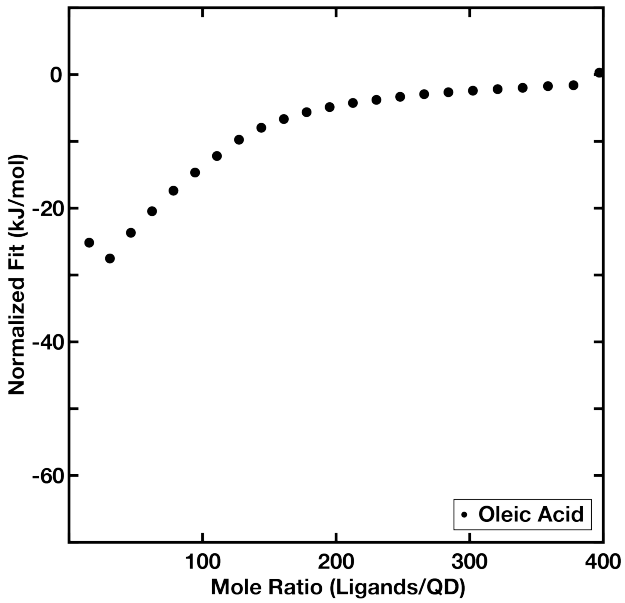

Figure 3.4: Integrated heats for oleic acid injection into InP QDs. The baseline corrected heat integrations for the addition of 31 mM oleic acid to InP QDs.

InP prepared and cleaned in this way, is underpassivated, as adding more ligand results in in a reasonable exothermic binding signal.

Moving on to the L type ligands, the plots for trioctylphosphine and oleylamine are shown in Figure 3.5. These ligands present a different binding moiety than the native X type (covalent bonding) ligands, so they should interact with the surface in different ways. The curve for trioctylphosphine shows a similar shape to the oleic acid curve, where an exothermic binding event quickly saturates the surface and produces no further signal. This would make sense in the model set up by the oleic acid data, where an underpassivated surface binds new ligands until it has saturated, but the thermodynamic curve produced by oleylamine changes this interpretation. Oleylamine addition produces a very large amount of heat, almost a factor of 4 greater than either the oleic acid or trioctylphosphine additions. Since the carbon chain of oleylamine is the same as that of oleic acid, this points to a difference in the head group of the ligands contributing the difference in the heats generated. Since both triocytlphosphine and oleylamine bind to QDs in an L type regime, it would be expected that they would show similar binding heats, as they should coordinate similar surface sites. Since the oleylamine signal is nearly seven times larger than the trioctylphosphine signal, it would suggest that the steric hindrance of the three octyl groups prevents the trioctylphosphine from interacting well with the surface and decreases the overall amount of ligand binding. Since the ability of the binding head group of a ligand to interact with the surface of the QD depends on how well the ligand can fit into the existing ligand shell, ligands with more steric hindrance will interact less with the surface and thus have less heat of reaction that could be detected by the ITC. The data that were observed suggests that there is a surface

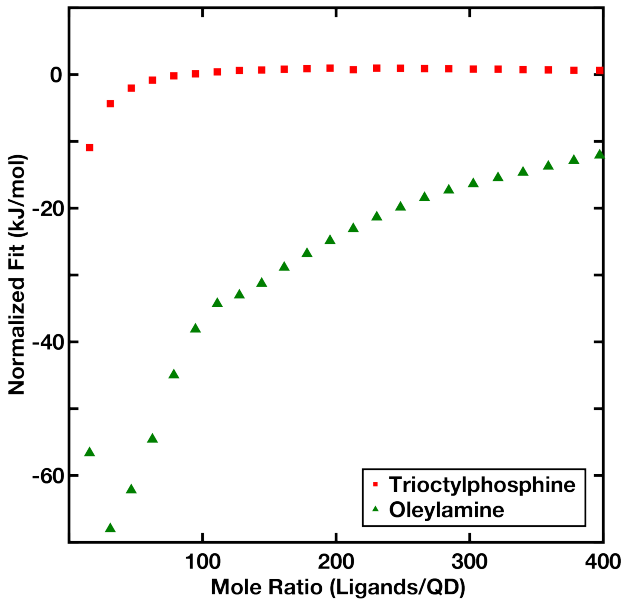

Figure 3.5: Integrated heats for oleylamine and trioctylphosphine injection into InP QDs. Both L type ligands show similar shapes to their binding energy, but the oleylamine shows a much larger total heat output.

site that oleylamine is able to strongly bind to that is inaccessible to either the carboxylate group of oleic acid or the stericly hindered lone pair of trioctylphosphine. Additionally, the data would suggest that oleylamine binds the strongest of these ligands to the InP surface, as it produces the most energy upon addition. It should be noted that in each of these cases, the ligands show as simple binding curve, where the signal increases until the ligand addition saturates the surface of the QD.

The outlier of this data is the curve generated by hexylphosphonic acid, seen in Figure 3.6. The curve generated by the addition of hexylphosphonic acid does not show the monotonic, exothermic binding that is seen in the other ligands, but instead shows a different, more complex exothermic process. This shape could be from a variety of factors, but the most likely culprit is that toluene appears to be a poor solvent for the addition of hexylphosphonic acid, as it takes a long time for the baseline to come down after the addition of the hexylphosphonic acid. Changing the solvent from toluene to another, better solvent such as tetrahydrofuran would clear this issue and likely produce a simpler and more interpretable ITC thermodynamic curve. This is beyond the scope of this work, as changing the solvent requires all previous data to be retaken in that new solvent, but future work in this field will likely be able to clarify the exact process of phosphonic acid binding to the surface of InP QDs. It is interesting that, despite the ITC data not being perfectly clear, the addition of the phosphonic acid was the only ligand that visibly improved the PLQY of the QDs, so additional study of these ligands is important to understand how and why they behave as they do.

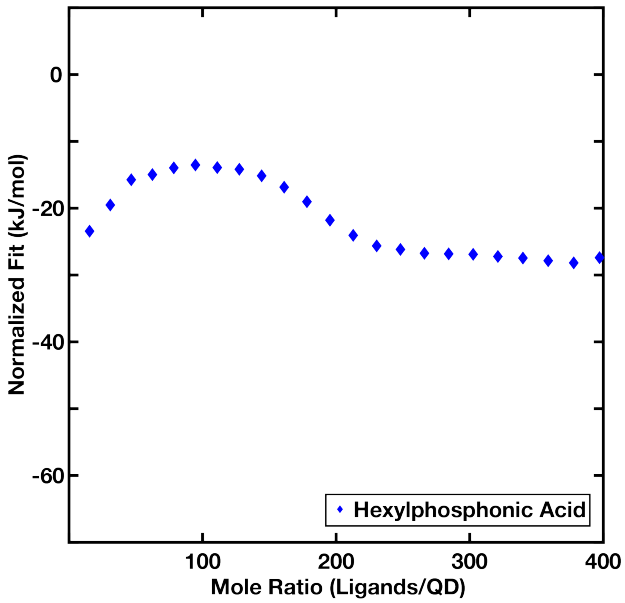

Figure 3.6: Integrated heats for hexylphosphonic acid injection into InP QDs. The strange shape of the curve is likely due to a combination of head group effects and solvent issues.

While ITC thermodynamic data gives the heat released by a ligand binding event, it does not give any information about the surface coverage of the QD. To complement the thermodynamic heats, NMR was used to learn about the ligand coverage of the InP QDs before and after additional ligands were added.

3.5 Nuclear Magnetic Resonance Spectroscopy for the Determination of Surface Ligand Coverage of Indium Phosphide Quantum Dots

NMR Quantification of the Addition of Ligands to Indium Phosphide Quantum Dots

Using the same type of NMR characterization as in the quantification of the native ligand shell, the ligand shell of QDs that had been treated with carboxylate and amine ligands was investigated. These ligands were chosen because at the center of each of their carbon chain tails is a double bond that provides a convenient NMR handle. This double bond appears around 5.5 ppm in the ^{1}H NMR spectrum, well separated from both the saturated protons of the ligand and the aromatic protons of the mesitylene standard. This separation, combined with the fact that ligands that are bound to the surface of the QD exhibit a broader signal in the NMR due to the relatively slow movement of the QD as compared to free ligand,[123]

allows for an accurate determination of the amount of bound ligand on the surface of the QD by integrating and comparing the areas of the broad, bound fraction with that of the sharp, unbound fraction. A summary of the fractional composition of the ligand shell can be found in Table 3.1. The solutions that were used for NMR quantification were made to replicate the conditions of a finished ITC run. That is to say, the same number of QDs as in an ITC run were dried, resuspended in deuterated toluene, and the equivalent amount of ligand to 23 10 μL injections was added and allowed to react. This process is detailed in Appendix B.

Sample	Native Myristic Acid (%)	Oleylamine (%)	Oleic Acid (%)
Native	100	0	0
Oleic Acid Addition	84	0	16
Oleylamine Addition	56	44	0
Oleylamine Addition, Washed Once	34	66	0
Oleylamine Addition, Washed Twice	99	1	0

Table 3.1: Quantification of the surface ligand fractions for various ligand additions.

It was found that when oleic acid, a carboxylate ligand, was added to the QD solutions, not all of the ligand binds, as seen in Figure 3.7. This is rationalized by remembering that the native ligands of the QDs are also carboxylate ligands. As such, most of the surface of the QD that has a binding site for a carboxylate would already have one bound to it, as there is an excess of ligand left over from the synthesis of the QDs. The only sites that should have an open location for the carboxylate ligands should be ones where the ligand was removed during the cleaning process, which should not be a large fraction of the QD surface. The total ligand shell ends up being 84% native ligand and 16% added oleic acid, as seen in Table 3.1. This also is in agreement with the ITC data where, by the end of the run, the heat generated by adding more oleic acid is minimal, which indicates that the reaction has gone to completion.

Amines, on the other hand, present a different binding moiety to the carboxylate ligands and should be able to access alternate surface sites. When oleylamine is added to the QD solution in the same way as the aforementioned oleic acid, it is found to bind quantitatively for the amount that is used in an ITC experiment. This is to say, when amines are added to the QD solution, the NMR shows that all of the amines bind to the QD and exhibit the broadened signal seen in Figure 3.8. This is an important finding, as it confirms that the strong binding signal seen in the ITC is due to the amine ligands interacting strongly with the InP QD's surface. Additionally, by quantifying the amount of bound amine in Table 3.1, one can see that the amine accounts for 44% of the bound ligand, while the native myristic acid makes up the other 56%. This shows that the amines are finding surface sites that the native carboxylates are unable to bind to as, dispute making up almost half of the bound ligands, there is no displacement of the native myristate ligands seen between 1 and 1.5 ppm in Figure 3.8.

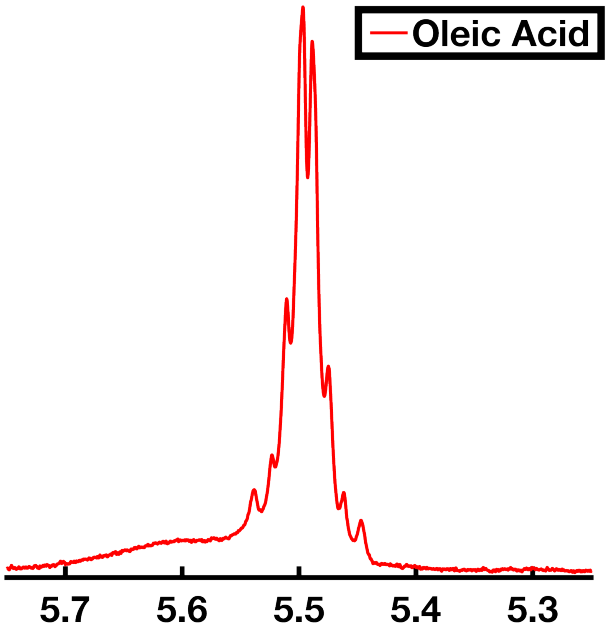

Figure 3.7: NMR of the unsaturated hydrogens of oleic acid after addition of a solution of InP QDs. Note that there are peaks representing two populations, a bound fraction (broad) and an unbound fraction (sharp multiplet).

NMR Investigation of Washing Effects on the Ligand Shell of Indium Phosphide Quantum Dots

In addition to studying the addition of new ligand to the surface of InP, the effect of washing on the composition of the ligand shell was also investigated. Since amine ligands have shown both larger heats of reaction as well as more complete binding, it was expected that they should survive the washing process better than the native carboxylate ligands. The native ligands are known to be removed by washing, as seen in both the literature[124] and in the addition of carboxylate ligands in section 3.5. The summary of the results can be seen in Table 3.1. After two washing steps detailed in section B.3, much of the ligand shell of the QD was removed, including all of the added oleylamine, but NMR taken after only one washing step showed a large amount of oleylamine still bound to the surface. In fact, the integration comparison shows that the fraction of oleylamine in the ligand shell increases from 44% to 66%. This means that while many ligands were removed in the washing process, most of them were carboxylates. The fact that the carboxylates remain after the second washing is likely only due to the fact that there were more of them to start with.

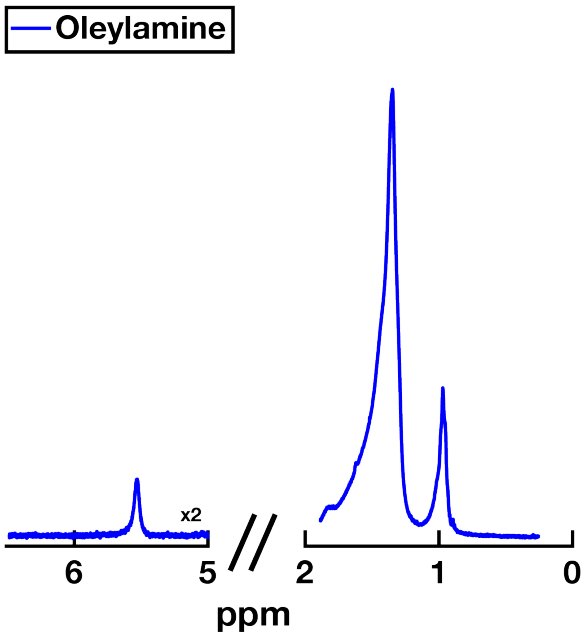

Figure 3.8: NMR of the unsaturated hydrogens of oleylamine after addition of a solution of InP QDs. The NMR spectrum of oleylamine does not show an unbound fraction in the peak around 5.5 ppm, nor does it show one in the aliphatic region below 2 ppm. The region of the 5.5 ppm peak has been doubled in height for clarity.

3.6 Conclusions

This work explored the interaction of various ligands with the surface of InP QDs. It was shown that the surface of InP QDs is accepting of a wide variety of post-synthetic ligands, with each of them demonstrating an exothermic signal upon being mixed with the QDs. This means that the ligands were able to form bonds with the surface of the QDs, and oleylamine was shown to be the ligand that produced the most heat of binding. The surface was further characterized via NMR, where it was shown that the surface of the QDs was underpassivated. The two ligands that were investigated, oleic acid and oleylamine, were shown to bind to the unpassivated surface sites, but oleylamine was shown to bind more fully to the surface. This indicates that the L type binding moiety of the oleylamine can access surface sites that X type carboxylates cannot, indicating that L type ligands are likely better passivants for InP QDs than other types of ligands.

Future directions of this work involve more detailed studies of the effects of different ligand attributes on the binding thermodynamics of ligands to InP QDs. Changing things like the length of the carbon chain of the ligand can inform the role that the tail of the ligand has in the binding efficiency, which was not studied in this work. Additionally, further NMR study on more types of ligand binding groups would fill out the picture of the surface of the QDs. Finally, expanding the types of ligands to be investigated to include inorganic ligands

such as $ZnCl_2$ would be interesting, as these ligands have been shown to greatly improve the optical properties of InP QDs but their thermodynamics have not been studied.

Appendix A

Synthetic Details

A.1 Materials

All materials (save the Schlenk line argon) were used as purchased with no further purification.

For the synthesis of InP quantum dots: indium (III) acetate (99.99%, Sigma-Aldrich), myristic acid (Sigma grade, 99%, Sigma-Aldrich), 1-octadecene (ODE, technical grade, 90%, Sigma-Aldrich), tris-(trimethylsilylphosphine) (TMSP, 98%, Strem Chemicals), and trioctylphosphine (TOP, 97%, Strem Chemicals).

Solvents and anitsolvents: acetone (anhydrous, 99%, Sigma-Aldrich), hexanes (anhydrous, 99%, Sigma-Aldrich), toluene (anhydrous, 99.8%, Sigma-Aldrich), ethanol (absolute, Sigma-Aldrich), chloroform (HPLC grade, Fischer Scientific), ethyl acetate (99.5%, Sigma-Aldrich), and isopropyl alchohol (anhydrous, 99.5%, Sigma-Aldrich).

Surface treatment reagents: tetrabutylammonium fluoride trihydrate (TBAF, 97%, Sigma-Aldrich) and hydrofluoric acid (HF, 48 wt% in water, $\geq$99.99% trace metals basis, Sigma-Aldrich).

Rare earth precursors: yttrium (III) oxide (99.99%, GFS Chemicals), ytterbium (III) oxide (99.9%, GFS Chemicals), neodymium (III) oxide (99.9%, GFS Chemicals), lutetium (III) oxide (99.9%, Alfa Aesar), trifuoroacetic acid (TFA, VWR Biotech grade, VWR), oleylamine (OLA, 98% primary amine, Sigma-Aldrich), and oleic acid (OA, technical grade, 90%, Sigma-Aldrich).

Schlenk line inert gas: argon (99.9995%, Praxair with additional Nupure purifier as specified the discussion below).

A.2 Core/Shell/Shell Nanoparticle Synthesis

InP Quantum Dot Synthesis

In a typical large scale reaction, indium (III) acetate (1.2 mmol, 350 mg), myristic acid (3.6 mmol, 822 mg) and ODE (10 mL) were charged into a 25 mL three neck flask and degassed/dried under vacuum at 110 °C for at least one hour (with a final vacuum pressure of ≤50 mTorr). The solution was then heated to 130 °C under ultra pure argon (discussed below in section A.3). In an argon glovebox kept at ≤0.5 ppm O_2, TMSP (0.6 mmol, 152 mg) was dissolved in TOP (1.66 g, for the rare earth addition work) or ODE (1.58 g, for the ligand characterization work). When InP was synthesized using TOP, the size dispersions were smaller and the reactions progressed slower than particles synthesized with ODE. This is likely due to the TOP slowing the reaction down, allowing for better control of the particle size. The TMSP and solvent (TOP or ODE) was shaken to combine, and then drawn up into a plastic Leur lock syringe with a 21 gauge needle (used to decrease the hold up volume of the syringe) and injected into the vigorously stirring $In(myristate)_3$ solution at 130 °C. The solution was allowed to react for 2 minutes at 130 °C before it was ramped to 230 °C at a rate of ∼25 °C/min (as fast as the heating mantle would heat). The reaction was held at 230 °C for 15 minutes before being cooled to room temperature by removing the heating mantle and blowing forced air over the outside of the flask. The solution was typically orange to deep red, and free from any insoluble species.

Cleaning InP Quantum Dots

After the InP reaction mixture was cooled to room temperature, it was transferred via cannula to a hot, dry, and air free Schlenk flask and then transferred into an argon glovebox (typically kept at ≤ 1 ppm O_2). Once inside, the solution was poured into a 50 mL centrifuge tube and precipitated with excess acetone (∼35 mL). The cloudy solution was then centrifuged at $8228g$ for 6-8 minutes and returned to the glovebox where the clear supernatant was decanted and removed. The resultant pellet was then resuspened in <5 mL hexanes. It should be noted that in some cases the quantum dots did not precipitate fully, and instead stayed suspended in a thick, darkly colored liquid at the bottom of the tube. In these cases, the supernatant is removed by careful decanting if the bottom solution is thick enough, or via syringe. The quantum dot solution was then diluted in ∼3 mL hexanes, and the cycle was continued as normal. The acetone precipitation-centrifugation-redispersion cycle was repeated, and the resultant cleaned quantum dots were stored in the glovebox for later characterization and use.

Surfance Treatment of InP Quantum Dots

Cleaned InP quantum dots were treated with TBAF to passivate the surface and provide an adhesion layer for the subsequent layer of rare earth fluorides. To do this, 100 nmol of

cleaned InP quantum dots (as determined by the absorption of the first excitonic peak)[67] in hexanes were removed from the glovebox and added to a solution of 32.5 mg of TBAF and 5μL of HF in 250μL of acetone. The mixture was vigorously stirred for $\sim$2 hours under bright visible light illumination. After this treatment, the solution separated into two phases. The clear top layer was discarded, while the viscous deeply colored bottom phase was immediately used for shelling.

Preparation of Stock Solutions for Shelling

For shelling InP quantum dots with rare earth fluorides, a multi-step procedure was emplyed to make the precursor solutions. First, 5 mmol of the desired rare earth oxide (Yb_2O_3, Y_2O_3, Lu_2O_3, or Nd_2O_3 for this work) was charged into a 100 mL three neck flask with two septa and one condenser column. Next, 50 mL of millipore water was added, followed by $\sim$15 mL of neat TFA. Caution should be taken in the addition of TFA, as it is a superacid, and is incredibly corrosive and the addition of the TFA to the water is very exothermic. The resultant cloudy solution was heated in an oil bath to 90 °C until all of the rare earth oxide was dissolved, typically overnight. The condenser column was necessary to prevent the water and TFA evaporating overnight. After all of the oxide dissolved, the water and excess TFA was removed by lowering the oil bath temperature to 65 °C and removing the septa and condenser column. Once the liquid evaporated, 10 mL OA, 10 mL ODE, and 2.5 mL OLA were added to the powder and the mixture was degassed under vacuum at 120 °C. Care should be taken in the application of vacuum to the mixture, as a significant amount of water is still bound to the rare earth trifluoroacetate. The solution was kept under vacuum for at least 2 hours, and resulted in a clear, viscous champagne colored solution. The solution was cannulated into a Schlenk flask and stored in an argon glovebox for future use.

Shelling with $Y_{1-x}Ln_xF_3$, where Ln = Yb, Nd

The example of $Y_{0.8}Yb_{0.2}F_3$ is given here, but the exact ratio of rare earth TFA precurors was changed to achieve the desired molar ratio for each reaction. A 50 mL three neck flask was charged with OLA (1 mL), ODE (7 mL), and 100 nmol of treated InP quantum dots and the solution was degassed at 100 °C until the baseline pressure of the Schlenk line was reached (typically <30 mTorr) for 1 hour. The treated quantum dots do not disperse well into ODE on their own, typically forming droplets of another phase within the ODE without the addition of the OLA. While the solution was degassing, the shelling solution was prepared in an argon glovebox. For this molar ratio, 73 μL of $Yb(TFA)_3$ stock solution, 223 μL of $Y(TFA)_3$ stock solution, and 1704 μL of ODE were mixed well in an argon glovebox before being drawn into a Leur lock syringe and removed from the glovebox. Since the shelling precursors are very thick, it is best to draw them into the syringe with a large bore needle, and then replace that needle with a small bore long needle. Once the initial solution finished degassing, it was placed under argon and ramped to 300 °C. When the solution reached

temperature, the shelling precursors were injected at the rate of 2 mL/hr with a syringe pump. After the injection finished (one hour later), the reaction was allowed to stay at temperature for an additional 5 minutes to allow all of the TFA precursor to react before it was cooled to room temperature by removing the heating mantle and blowing air over the flask.

Cleaning Core/Shell Nanoparticles

Once the reaction was cooled, it was placed into a 50 mL centrifuge tube and ∼35 mL of a 50/50 mixture of acetone and ethyl acetate was added. The ethyl acetate is necessary to prevent the solution from becoming biphasic. The resultant cloudy mixture was centrifuged at $8228g$ for 5-8 minutes, after which the clear supernatant was discarded from the nanoparticle pellet. The pellet was then redispersed in <5 mL hexanes and the process was repeated with ∼20 mL of acetone. The final mixture ranges in color from a light pink to a dark red depending on the final nanoparticle concentration. The solution was then left overnight so that insoluble impurities were allowed to crash out of solution, which allowed them to be removed.

Final shelling with LnF_3, where Ln = Y, Lu

For the final inert shelling, all of the core/shell nanoparticles from the previous shelling step were mixed into ODE (8 mL) in a 50 mL three neck flask and degassed at 100 °C for 1 hour. At the same time, the desired amounts of rare earth TFA (in this work, $Y(TFA)_3$ or $Lu(TFA)_3$) solution (2.25 mL) and ODE (1.75 mL) were mixed well in an argon glovebox. Since the TFA precursors are very viscous, special care needs to be taken to ensure that the solutions are mixed homogeneously into the ODE. The mixture was drawn into a Leur lock syringe with a large bore needle, and that needle was then replace with a long 21 guage needle for injection. Failure to do this results in it taking a very long time to get the solution into the syringe and this represents an ergonomic hazard, as prolonged syringe use in the glovebox is not good for hand health. The nanoparticle solution was heated to 300 °C, and the TFA solution was injected at 2 mL/hr using a syringe pump once the nanoparticle solution reached temperature. Once the injection finished, the solution was again allowed to further react for 5 minutes before the heating mantle was removed and air was blown over the reaction to cool it to room temperature. The final solution was typically light yellow in color. Though no OLA was typically added beyond that in the TFA solution, adding OLA was found to decrease the amount of nucleation of pure LnF_3 nanoparticles.

Cleaning Core/Shell/Shell Nanocrystals

The reaction mixture from the previous step was placed into a 50 mL centrifuge tube and precipitated with ∼35 mL of acetone. The cloudy white solution was then centrifuged

at $8228g$ for 6-8 minutes, affording an off white pellet and a clear supernatant. The supernatant was discarded, the pellet was redispersed in hexanes, and the process of precipitation-centrifugation-resupension was repeated with acetone-hexanes-minimal IPA-hexanes. The final IPA wash was needed to remove some impurites that remained in solution due to the solution becoming biphasic. The final clear product solution was typically light yellow or red in color.

Size-Selective Precipitation

The cleaned core/shell/shell nanoparticles from the previous step were size selectively precipitated to remove impurity particles and improve sample homogeneity. To do this, the desired amount of core/shell/shell solution was placed into a 15 mL centrifuge tube and acetone was added dropwise until the solution just becomes cloudy. The solution is then swirled, and the cloudiness dissipates. This process is repeated until swirling the solution no longer removes the cloudiness, at which point the cloudy solution was centrifuged at $8228g$ for 5 minutes. The pellet was collected by removal of the clear supernatant, and the processes was repeated. TEM and optical characterizations were used to determine which fraction was the desired fraction.

A.3 The Importance of Ultra-High Purity Argon in the Synthesis of InP Quantum Dots

The precise chemical composition of the surface of InP quantum dots is very important to the optical properties of the nanoparticles, the ability of Ln ions to adhere to the quantum dots, and obviously the ligand interactions with the quantum dot. It is well known that the surface of InP is oxidized, but the exact source and nature of that oxidation is not fully understood. In a previous iteration of Ln decorated InP research, instead of growing a LnF_3 shell around InP, attempts were made to incorporate Ln ions directly into the lattice of InP. These efforts were not successful, likely due to the unfavorability of Yb incorporation into the InP lattice and the Yb-P bond. However, it was found that Yb did adsorb onto the surface of the InP, resulting in some energy transfer and a moderate amount of emission from the Yb level at 976 nm. If the particles were allowed to sit in an inert glovebox for only a couple of days, the observed luminescence would completely vanish. This was presumably due to the Yb ions desorbing from the surface of the InP.

Also, EXAFS measurements of these samples showed that the Yb of very fresh samples was completely coordinated by oxygen atoms. This is somewhat unexpected, as the Yb should have some O coordination from the ligands and some P coordination from the InP quantum dot. This is true even of samples prepared on the same day and loaded inside of an inert atmosphere glovebox, meaning the oxygen was not likely due to atmospheric oxygen.

To combat this, and argon purifier (NuPure Model E-200-CAG Eliminator) was added to the Schlenk line argon supply. The specifications of this purifier placed the O_2 levels of

the line at sub-part-per-billion, which was orders of magnitude lower than the high purity argon from the cylinder (UHP, 99.9995%). When this addition was made it was found that, following the exact same reaction conditions, there was no observable NIR luminescence from the Yb. This is likely due to the removal of the surface oxygen from the InP making it harder to adsorb Yb.

Interestingly, at that level of argon purity, the single largest source of O_2 contamination for the Schlenk line was the 20 mTorr vacuum base pressure. If the highest level of oxygen purity is needed, it is best practice to pump-purge the reaction with a slightly modified procedure. Vacuum should be pulled down to ∼100 mTorr before the reaction is switched to argon, and the process should be repeated 3 times. This dilutes any oxygen present to the lowest possible levels for maximum purity.

In addition to being unable to affix Yb to the surface of the InP quantum dots after adding the oxygen purifier, the properties of the InP itself changed as well. It was found that O_2 free InP had a much lower PLQY than InP synthesized under UHP or standard (99.9%) argon, typically <0.1% versus ∼5%. This decrease in PLQY along with the inability to affix Yb ions to the surface of InP grown under essentially O_2 free argon suggests that all InP quantum dots have a shell of In_2O_3 that poorly passivates the surface of the quantum dots and significantly changes the optical properties of the quantum dots. The full magnitude of this effect has not been well explored, but seeing the size of the effect it is certainly something that deserves further study.

Appendix B

Characterization Methods

B.1 Structural Characterization Methods

TEM Characterization

For low-resolution TEM imaging, an FEI Tecnai T20 S-TWIN TEM operating at 200kV with a LaB_6 filament. Images were collected with a Gatan Orius SC200 camera at 2k x 2k resolution.

High resolution (HRTEM) images and basic scanning electron microscopy (STEM) images were taken on a JEOL 2100-F microscope operating at 200 kV with a field emission gun source.

Elemental mapping (STEM-EDS) was performed on an FEI Titan 80-300 kV microscope operated at 200 kV with a prove current of 600 nA at the National Center for Electron Microscopy, Molecular Foundry, Lawrence Berkeley National Lab (NCEM at LBNL). The STEM images were taken using a Fischione high-angle annular dark-field (HAADF) detector with an inner semi-angle of 59 mrad. The EDS detector was an FEI Super-X Quad windowless detector operating with a solid angle of detection of 0.7 steradians. Bruker Esprit software was then used for the quantitative analysis.

Powder X-Ray Diffraction

Powder XRD measurements were taken using a Bruker D-8 GADDS diffractometer with a Co kα source.

EXAFS Measurements

Extended x-ray absorption fine structure (EXAFS) measurements were taken on beamline 10.3.2 of the Advanced Light Source (ALS) at LBNL. The beamline was equipped with a bending magnet capable of producing x-rays from 2.1-17 keV, and the ALS storage ring operates at 500 mA of current at 1.8 GeV. Sample pellets were prepared by precipitating

them from solution via ethanol addition and centrifugation (ethanol was chosen to precipitate as many particles as possible from solution). The pellet was then trapped in a piece of Kapton tape. The samples were then placed into a hole in an aluminum mounting plate, mounted into the beamline, and the signal was detected via the x-ray flolurescence of the sample. The XANES/EXAFS spectra were taken over the range of 8845 eV to 9946 eV. Data analysis was first performed using custom processing softwore produced by the staff scientists of 10.3.2 to correct for energy drift, detector deadtime, and glitching. The data was the further processed and fit using Artemis and Athena.[125]

B.2 Optical Characterization

Steady State Optical Measurements

Steady state absorbance measurements were taken on a Shimadzu UV-3600 double beam spectrometer operating with 1 nm slits at the second slowest setting.

Steady state flourescence measurements were taken on two instruments. The first was a home built integrating sphere setup, the details of which can be found in the SI of Bronstein *et al.*,[126] but a brief description will be given here. A Fianium SC450 supercontinuum pulsed laser provided a white light source with an average illumination intensity of 4 W from 410 nm to 2500 nm. The precise excitation wavelength was selected by passing the beam through two monochromators, a Princeton Instruments SP150 and a Princeton Instruments SP275. After wavelength selection was performed, the beam was sent through a beamsplitter to a calibrated photodiode to constantly measure the power of the beam, and the majority of the light was directed into the 25-mm entrance port of a 135 mm Spectralon integrating sphere from LabSphere. The sample was held using a custom built Spectralon circular cuvette holder on the opposite side of the sphere from the excitation. In addition to the tunable source, a second single wavelength laser was positioned to bypass the monochromators and enter thru the same port of the integrating sphere. The second laser was a Power Technology LDCU 12/6692 laser that emitted at 440 nm with a max power of 16 mW. The second laser was also passed through a beamsplitter to a photodiode to monitor the power. PLQY values used in the paper used an excitation power of 9.7 mW over $\sim$1 mm^2 and were calculated by integrating the counts of the NIR Yb emission then comparing that value to the absorbed light at 440 nm. Direct reflections were blocked from exiting the sphere by a baffle, ensuring only diffuse light escaped the integrating sphere. The light exiting the sphere was focused onto the entrance slit of a Princeton Instruments SP2300 monochromator with a 300 g/mm grating blazed at 500 nm. The resultant spectrum was detected with either a Princeton Instruments PIXIS 400 B thermoelectrically cooled (TE) silicon CCD or an Andor iDus InGaAs (1.7 μm) camera. The CCD had been corrected for both spectral position using a HeNe lamp and for sensitivity using a NIST-traceable radiometric calibration lamp from Ocean Optics, model HL3-plus, serial number 089440003.

The second setup that was used was an Edinburgh Instruments FLS980 equipped with

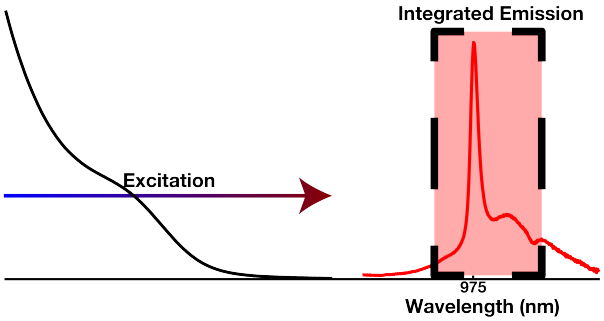

Figure B.1: Cartoon schematic of an excitation scan. The detection wavelength range is kept constant while the excitation is scanned across the nanoparticle absorption.

a 450 W Xe-lamp and a single monochromator with two holographic gratings; 1800 g/mm blazed at 250 nm and 1200 g/mm blazed at 750 nm as an excitation source. The detection monochromator had three gratings; 1800 g/mm blazed at 500 nm, 1200 g/mm blazed at 750 nm, and 830 g/mm blazed at 1200 nm. Two photomultiplier tubes manufactured by Hamamatsu were attached, but only the TE-cooled R2658P with a spectral range of 200-1010 nm and a detector response of 800 ps was used. The system was calibrated for sensitivity by Edinburg Instruments.

Excitation Scans

Excitation scans were performed on the aforementioned Edinburg Instruments FL980. This measurement is valuable to determine if an observed emission event is related to the absorption of the sample. A cartoon schematic of this process is found in Figure B.1. The detection monochrometer was centered at the middle of the 976 nm emission peak of Yb with a bandwidth of 10 nm (to capture the entire peak). The excitation wavelength was then scanned from 400-800 nm in 1 nm steps, and the integrated intensity of the emission peak was recorded. The excitation spectrum was then compared to the absorbance factor/absorptance (linear scale) of the sample, found by the following relation to the absorption (log scale), which is what is typically reported.

$$Absorption\ Factor = 1 - 10^{-Absorption}$$

Once this has been done, the two lines are normalized to the first excitation peak and plotted against each other to form the plot found in Figure 2.14.

Time-Resolved Photoluminescense

Time resolved photoluminescence (TRPL) measurements for the visible band edge emission of InP quantum dots were taken using a PicoQuant Fluotime 300 equipped with a PMA 175 detector and a LDH-P-C-405 diode laser with an excitation wavelenght of 407.1

nm. While the laser was capable of achieving repetition rates of up to 80 MHz, lower repetition rates were used to observe the full decay of the photoluminescence.

TRPL measurements of the NIR lifetimes of Yb were taken on the aforementioned Edinburgh PLS980. The pump used was a Nd:YAG pumped optical parametric oscillator, the Opolette HE 355 LD from Opotek. This source covered a wavelenth range of 410-2200 nm with a laser pulse lenght of $\sim$7 ns and a repetition rate of up to 20 Hz.

B.3 NMR Characterization

Nuclear magnetic resonance spectra were aquired on the UC Berkeley College of Chemistry NMR facility AVQ-400, a Bruker AMX-400 magnet equipped with a Z-gradient 5 mm QNP probe. For each NMR measurement, the 90° pulse was checked while measurements were acquired using the 30° pulse and at least 16 scans were averaged with a D1 delay time of at least 5 seconds. Deuterated toluene used as the NMR solvent was stored in an inert atmosphere dry box.

Washing InP Quantum Dots for NMR Washing Studies

Samples for the study of the effect of washing on the ligand coverage of amine exchanged quantum dots, as described in section 3.5, were produced as follows. InP QD solution equivalent to 114 nmol of QDs was removed from the glovebox in a sealed septum-capped vial. The vial was brought to the Schlenk line, where ultra high purity argon was blown over the sample to remove the solvent. After the quantum dots were thoroughly dried, they were returned to the glovebox and resuspended in 1.8 mL of deuterated toluene and separated into three samples. Then 230 μL of 31 mM oleylamine in deuterated toluene was added to each InP solution and allowed to equilibrate for one hour. The first solution was placed directly into an NMR tube, while the second and third solutions were cleaned by adding roughly 3 mL of acetone to the 600 μL InP solution, centrifuged at $8228g$ for 7 minutes, and resuspended into 600 μL of deuterated toluene. The second InP solution was then placed into an NMR tube, and the antisolvent addition-centrifugation-resuspension process was repeated one final time for the third InP solution.

B.4 ITC Methodologies

Thermodynamic ITC data was taken using a TA instruments Nano ITC equipped with a gold sample cell. This instrument injects a small amount of titrant into a sample cell kept at a constant temperature under stirring. The instrument then detects the amount of heat that is needed to keep the sample cell at that same constant temperature versus how much energy is needed to keep a reference cell at that temperature. The process results in a plot of heat rate versus time as seen in Figure B.2 A. The signal can be integrated over the time that corresponds with each injection and a total amount of heat per injection can be calculated,

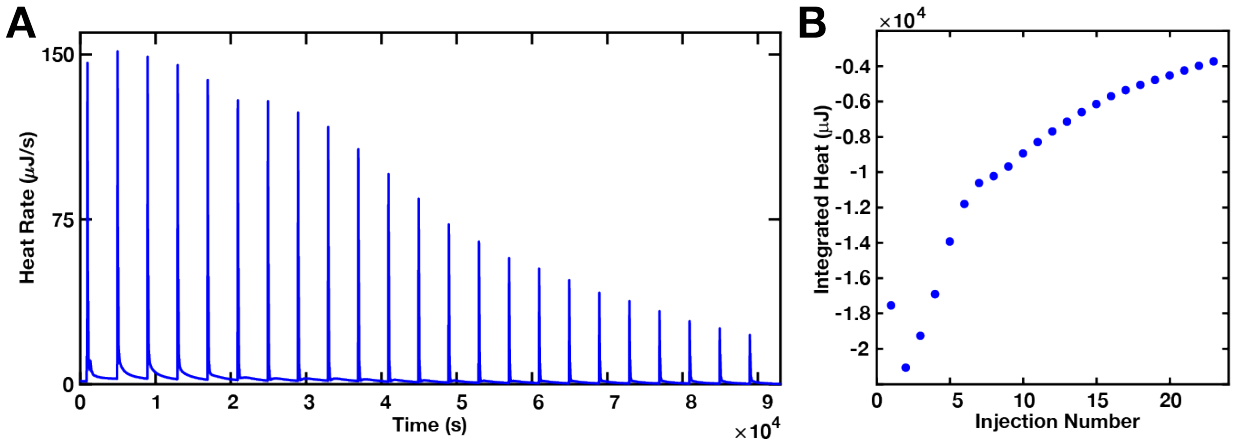

Figure B.2: Example of the raw and integrated data from the ITC. (A) A plot of the observed heat rate versus time for a ligand injection into InP QD. Note that the reaction returns to the baseline value each time, though the process is slow. (B) Heat values found by integrating the raw plot in A with respect to time. The first point of ITC data tends to be inconsistent, and should not be used for analysis.

which is shown in Figure B.2 B. A standard experiment was allowed to equilibrate for at least 2000 seconds in order to make sure that any reaction between the ligands and the QDs in the sample cell had time to reach equilibrium, though frequently a 3600 second eqilibration time was needed.

The process of injecting titrant into the ITC cell is done for a blank (ligand and solvent injected into solvent) and a sample (ligand and solvent injected into a QD solution). The integrated heat values of the blank can be subtracted from the signal given from the QD to give a accurate value of the heat of the ligand addition reaction.

All ITC experiments were performed by injecting a solution of 31 mM ligand in anhydrous glovebox toluene into a 1.2 mL solution of 38 nmol of InP QDs in toluene. There were 23 injection of 10 μL each, which were stirred at 250 rpm at room temperature.

Bibliography

(1) Jasieniak, J.; Califano, M.; Watkins, S. E. Size-Dependent Valence and Conduction Band-Edge Energies of Semiconductor Nanocrystals. *ACS Nano* **July 2011**, *5*, 5888–5902.

(2) Kriegel, I.; Jiang, C.; Rodríguez-Fernández, J.; Schaller, R. D.; Talapin, D. V.; da Como, E.; Feldmann, J. Tuning the Excitonic and Plasmonic Properties of Copper Chalcogenide Nanocrystals. *Journal of the American Chemical Society* **Jan. 2012**, *134*, 1583–1590.

(3) Pelton, M.; Aizpurua, J.; Bryant, G. Metal-nanoparticle plasmonics. *Laser & Photonics Review* **July 2008**, *2*, 136–159.

(4) Tolbert, S. H.; Alivisatos, A. P. Size Dependence of a First Order Solid-Solid Phase Transition: The Wurtzite to Rock Salt Transformation in CdSe Nanocrystals. *Science* **July 1994**, *265*, 373–376.

(5) Tolbert, S. H.; Alivisatos, A. P. The wurtzite to rock salt structural transformation in CdSe nanocrystals under high pressure. *The Journal of Chemical Physics* **Mar. 1995**, *102*, 4642–4656.

(6) Rivest, J. B.; Fong, L.-K.; Jain, P. K.; Toney, M. F.; Alivisatos, A. P. Size Dependence of a Temperature-Induced Solid-Solid Phase Transition in Copper(I) Sulfide. *The Journal of Physical Chemistry Letters* **Oct. 2011**, *2*, 2402–2406.

(7) Dick, K. A.; Caroff, P.; Bolinsson, J.; Messing, M. E.; Johansson, J.; Deppert, K.; Wallenberg, L. R.; Samuelson, L. Control of III-V nanowire crystal structure by growth parameter tuning. *Semiconductor Science and Technology* **2010**, *25*, 024009.

(8) Jiang, H.; Moon, K.-S.; Dong, H.; Hua, F.; Wong, C. Size-dependent melting properties of tin nanoparticles. *Chemical Physics Letters* **Oct. 2006**, *429*, 492–496.

(9) Bogdan, N.; Vetrone, F.; Ozin, G. A.; Capobianco, J. A. Synthesis of Ligand-Free Colloidally Stable Water Dispersible Brightly Luminescent Lanthanide-Doped Upconverting Nanoparticles. *Nano Letters* **Feb. 2011**, *11*, 835–840.

(10) Gerion, D.; Pinaud, F.; Williams, S. C.; Parak, W. J.; Zanchet, D.; Weiss, S.; Alivisatos, A. P. Synthesis and Properties of Biocompatible Water-Soluble Silica-Coated CdSe/ZnS Semiconductor Quantum Dots. *The Journal of Physical Chemistry B* **Sept. 2001**, *105*, 8861–8871.

(11) Larson, D. R. Water-Soluble Quantum Dots for Multiphoton Fluorescence Imaging in Vivo. *Science* **May 2003**, *300*, 1434–1436.

(12) Pradhan, N.; Adhikari, S. D.; Nag, A.; Sarma, D. D. Luminescence , Plasmonic , and Magnetic Properties of Doped Semiconductor Nanocrystals Angewandte. **2017**, 7038–7054.

(13) Katari, J. E. B.; Colvin, V. L.; Alivisatos, A. P. X-ray Photoelectron Spectroscopy of CdSe Nanocrystals with Applications to Studies of the Nanocrystal Surface. *The Journal of Physical Chemistry* **Apr. 1994**, *98*, 4109–4117.

(14) Empedocles, S. A.; Norris, D. J.; Bawendi, M. G. Photoluminescence spectroscopy of single CdSe nanocrystallite quantum dots. *Physical Review Letters* **1996**, *77*, 3873–3876.

(15) Murray, C. B.; Norris, D. J.; Bawendi, M. G. Synthesis and characterization of nearly monodisperse CdE (E = sulfur, selenium, tellurium) semiconductor nanocrystallites. *Journal of the American Chemical Society* **Sept. 1993**, *115*, 8706–8715.

(16) Peng, X.; Manna, L.; Yang, W.; Wickham, J.; Scher, E.; Kadavanich, A.; Alivisatos, A. P. Shape control of CdSe nanocrystals. *Nature* **Mar. 2000**, *404*, 59–61.

(17) Harrison, M. T.; Kershaw, S. V.; Burt, M. G.; Rogach, A. L.; Kornowski, A.; Eychmüller, A.; Weller, H. Colloidal nanocrystals for telecommunications. Complete coverage of the low-loss fiber windows by mercury telluride quantum dot. *Pure and Applied Chemistry* **Jan. 2000**, *72*, 295–307.

(18) Kershaw, S. V.; Burt, M.; Harrison, M.; Rogach, A.; Weller, H.; Eychmüller, A. Colloidal CdTe/HgTe quantum dots with high photoluminescence quantum efficiency at room temperature. *Applied Physics Letters* **1999**, *75*, 1694–1696.

(19) Mićić, O. I.; Sprague, J.; Lu, Z.; Nozik, A. J. Highly efficient band-edge emission from InP quantum dots. *Applied Physics Letters* **1996**, *68*, 3150–3152.

(20) Battaglia, D.; Peng, X. Formation of High Quality InP and InAs Nanocrystals in a Noncoordinating Solvent. *Nano Letters* **Sept. 2002**, *2*, 1027–1030.

(21) Olshavsky, M. A.; Goldstein, A. N.; Alivisatos, A. P. Organometallic synthesis of gallium-arsenide crystallites, exhibiting quantum confinement. *Journal of the American Chemical Society* **Dec. 1990**, *112*, 9438–9439.

(22) Machol, J.; Wise, F.; Patel, R.; Tanner, D. Optical studies of IV-VI quantum dots. *Physica A: Statistical Mechanics and its Applications* **June 1994**, *207*, 427–434.

(23) Moreels, I.; Lambert, K.; De Muynck, D.; Vanhaecke, F.; Poelman, D.; Martins, J. C.; Allan, G.; Hens, Z. Composition and Size-Dependent Extinction Coefficient of Colloidal PbSe Quantum Dots. *Chemistry of Materials* **Dec. 2007**, *19*, 6101–6106.

(24) Murray, C. B.; Sun, S.; Gaschler, W.; Doyle, H.; Betley, T. A.; Kagan, C. R. Colloidal synthesis of nanocrystals and nanocrystal superlattices. *IBM Journal of Research and Development* **Jan. 2001**, *45*, 47–56.

(25) Warner, J. H.; Hoshino, A.; Yamamoto, K.; Tilley, R. D. Water-Soluble Photoluminescent Silicon Quantum Dots. *Angewandte Chemie International Edition* **July 2005**, *44*, 4550–4554.

(26) Erogbogbo, F.; Yong, K.-T.; Roy, I.; Xu, G.; Prasad, P. N.; Swihart, M. T. Biocompatible Luminescent Silicon Quantum Dots for Imaging of Cancer Cells. *ACS Nano* **May 2008**, *2*, 873–878.

(27) Protesescu, L.; Yakunin, S.; Bodnarchuk, M. I.; Krieg, F.; Caputo, R.; Hendon, C. H.; Yang, R. X.; Walsh, A.; Kovalenko, M. V. Nanocrystals of Cesium Lead Halide Perovskites ($CsPbX_3$, X = Cl, Br, and I): Novel Optoelectronic Materials Showing Bright Emission with Wide Color Gamut. *Nano Letters* **June 2015**, *15*, 3692–3696.

(28) Jang, E.; Jun, S.; Jang, H.; Lim, J.; Kim, B.; Kim, Y. White-Light-Emitting Diodes with Quantum Dot Color Converters for Display Backlights. *Advanced Materials* **May 2010**, *22*, 3076–3080.

(29) Kim, T. H.; Cho, K. S.; Lee, E. K.; Lee, S. J.; Chae, J.; Kim, J. W.; Kim, D. H.; Kwon, J. Y.; Amaratunga, G.; Lee, S. Y.; Choi, B. L.; Kuk, Y.; Kim, J. M.; Kim, K. Full-colour quantum dot displays fabricated by transfer printing. *Nature Photonics* **2011**, *5*, 176–182.

(30) Wood, V.; Panzer, M. J.; Chen, J.; Bradley, M. S.; Halpert, J. E.; Bawendi, M. G.; Bulović, V. Inkjet-Printed Quantum Dot-Polymer Composites for Full-Color AC-Driven Displays. *Advanced Materials* **June 2009**, *21*, 2151–2155.

(31) Wood, V.; Panzer, M.; Sullivan, S.-C.; Bulović, V. In *Colloidal Quantum Dot Optoelectronics and Photovoltaics*, Konstantatos, G., Sargent, E. H., Eds.; Cambridge University Press: Cambridge, 2010; Vol. 9780521198, pp 148–172.

(32) Song, J.; Li, J.; Li, X.; Xu, L.; Dong, Y.; Zeng, H. Quantum Dot Light-Emitting Diodes Based on Inorganic Perovskite Cesium Lead Halides ($CsPbX_3$). *Advanced Materials* **Nov. 2015**, *27*, 7162–7167.

(33) Caruge, J. M.; Halpert, J. E.; Wood, V.; Bulović, V.; Bawendi, M. G. Colloidal quantum-dot light-emitting diodes with metal-oxide charge transport layers. *Nature Photonics* **Apr. 2008**, *2*, 247–250.

(34) Shirasaki, Y.; Supran, G. J.; Bawendi, M. G.; Bulović, V. Emergence of colloidal quantum-dot light-emitting technologies. *Nature Photonics* **Jan. 2013**, *7*, 13–23.

(35) Bruchez Jr., M. Semiconductor Nanocrystals as Fluorescent Biological Labels. *Science* **Sept. 1998**, *281*, 2013–2016.

(36) Huynh, W. U. Hybrid Nanorod-Polymer Solar Cells. *Science* **Mar. 2002**, *295*, 2425–2427.

(37) Nozik, A. Quantum dot solar cells. *Physica E: Low-dimensional Systems and Nanostructures* **Apr. 2002**, *14*, 115–120.

(38) Skylar-Scott, M. A.; Gunasekaran, S.; Lewis, J. A. Laser-assisted direct ink writing of planar and 3D metal architectures. *Proceedings of the National Academy of Sciences* **May 2016**, *113*, 6137–6142.

(39) Ko, S. H.; Chung, J.; Hotz, N.; Nam, K. H.; Grigoropoulos, C. P. Metal nanoparticle direct inkjet printing for low-temperature 3D micro metal structure fabrication. *Journal of Micromechanics and Microengineering* **Dec. 2010**, *20*, 125010.

(40) Goetzberger, A.; Greube, W. Solar energy conversion with fluorescent collectors. *Applied Physics* **Oct. 1977**, *14*, 123–139.

(41) Weber, W. H.; Lambe, J. Luminescent greenhouse collector for solar radiation. *Applied Optics* **Oct. 1976**, *15*, 2299.

(42) Yablonovitch, E. Thermodynamics of the fluorescent planar concentrator. *Journal of the Optical Society of America* **1980**, *70*, 1362.

(43) Needell, D. R.; Ilic, O.; Bukowsky, C. R.; Nett, Z.; Xu, L.; He, J.; Bauser, H.; Lee, B. G.; Geisz, J. F.; Nuzzo, R. G.; Alivisatos, A. P.; Atwater, H. A. Design Criteria for Micro-Optical Tandem Luminescent Solar Concentrators. *IEEE Journal of Photovoltaics* **Nov. 2018**, *8*, 1560–1567.

(44) Kim, T.-G.; Zherebetskyy, D.; Bekenstein, Y.; Oh, M. H.; Wang, L.-W.; Jang, E.; Alivisatos, A. P. Trap Passivation in Indium-Based Quantum Dots through Surface Fluorination: Mechanism and Applications. *ACS Nano* **Nov. 2018**, *12*, 11529–11540.

(45) Azad Malik, M.; O'Brien, P.; Revaprasadu, N. Synthesis of TOPO-capped Mn-doped ZnS and CdS quantum dots. *Journal of Materials Chemistry* **2001**, *11*, 2382–2386.

(46) Bhargava, R.; Gallagher, D.; Hong, X.; Nurimkko, A. Optical Properties of Manganese-Doped of ZnS. *Physical Review Letters* **1994**, *72*, 1–4.

(47) Bol, A. A.; Meijerink, A. Long-lived Mn^{2+} emission in nanocrystalline ZnS:Mn^{2+}. *Physical Review B* **Dec. 1998**, *58*, R15997–R16000.

(48) Beaulac, R.; Archer, P. I.; Liu, X.; Lee, S.; Salley, G. M.; Dobrowolska, M.; Furdyna, J. K.; Gamelin, D. R. Spin-Polarizable Excitonic Luminescence in Colloidal Mn^{2+}-Doped CdSe Quantum Dots. *Nano Letters* **Apr. 2008**, *8*, 1197–1201.

(49) Parobek, D.; Roman, B. J.; Dong, Y.; Jin, H.; Lee, E.; Sheldon, M.; Son, D. H. Exciton-to-Dopant Energy Transfer in Mn-Doped Cesium Lead Halide Perovskite Nanocrystals. *Nano Letters* **2016**, *16*, PMID: 27797528, 7376–7380.

(50) Yang, J. et al. Route to the Smallest Doped Semiconductor: Mn^{2+}-Doped $(CdSe)_{13}$ Clusters. *Journal of the American Chemical Society* **Oct. 2015**, *137*, 12776–12779.

(51) Gumlich, H.-E. Electro- and photoluminescence properties of Mn^{2+} in ZnS and ZnCdS. *Journal of Luminescence* **1981**, *23*, 73–99.

(52) Panda, S. K.; Hickey, S. G.; Demir, H. V.; Eychmüller, A. Bright White-Light Emitting Manganese and Copper Co-Doped ZnSe Quantum Dots. *Angewandte Chemie International Edition* **May 2011**, *50*, 4432–4436.

(53) Wang, X.; Yan, X.; Li, W.; Sun, K. Doped Quantum Dots for White-Light-Emitting Diodes Without Reabsorption of Multiphase Phosphors. *Advanced Materials* **May 2012**, *24*, 2742–2747.

(54) Dalpian, G. M.; Chelikowsky, J. R. Self-Purification in Semiconductor Nanocrystals. *Physical Review Letters* **June 2006**, *96*, 226802.

(55) Ondry, J. C.; Hauwiller, M. R.; Alivisatos, A. P. Dynamics and Removal Pathway of Edge Dislocations in Imperfectly Attached PbTe Nanocrystal Pairs: Toward Design Rules for Oriented Attachment. *ACS Nano* **Apr. 2018**, *12*, 3178–3189.

(56) Veamatahau, A.; Jiang, B.; Seifert, T.; Makuta, S.; Latham, K.; Kanehara, M.; Teranishi, T.; Tachibana, Y. Origin of surface trap states in CdS quantum dots: relationship between size dependent photoluminescence and sulfur vacancy trap states. *Physical Chemistry Chemical Physics* **2015**, *17*, 2850–2858.

(57) Voznyy, O.; Thon, S. M.; Ip, A. H.; Sargent, E. H. Dynamic Trap Formation and Elimination in Colloidal Quantum Dots. *The Journal of Physical Chemistry Letters* **Mar. 2013**, *4*, 987–992.

(58) Reich, K. V.; Shklovskii, B. I. Exciton Transfer in Array of Epitaxially Connected Nanocrystals. *ACS Nano* **Nov. 2016**, *10*, 10267–10274.

(59) Fischer, S.; Bronstein, N. D.; Swabeck, J. K.; Chan, E. M.; Alivisatos, A. P. Precise Tuning of Surface Quenching for Luminescence Enhancement in Core-Shell Lanthanide-Doped Nanocrystals. *Nano Letters* **2016**, *16*, 7241–7247.

(60) Nikoobakht, B.; Burda, C.; Braun, M.; Hun, M.; El-Sayed, M. A. The Quenching of CdSe Quantum Dots Photoluminescence by Gold Nanoparticles in Solution. *Photochemistry and Photobiology* **2002**, *75*, 591.

(61) Bimberg, D.; Grundmann, M.; Ledentsov, N.; Ruvimov, S.; Werner, P.; Richter, U.; Heydenreich, J.; Ustinov, V.; Kop'ev, P.; Alferov, Z. Self-organization processes in MBE-grown quantum dot structures. *Thin Solid Films* **Oct. 1995**, *267*, 32–36.

(62) Mews, A.; Eychmueller, A.; Giersig, M.; Schooss, D.; Weller, H. Preparation, characterization, and photophysics of the quantum dot quantum well system cadmium sulfide/mercury sulfide/cadmium sulfide. *The Journal of Physical Chemistry* **Jan. 1994**, *98*, 934–941.

(63) Dabbousi, B. O.; Rodriguez-Viejo, J.; Mikulec, F. V.; Heine, J. R.; Mattoussi, H.; Ober, R.; Jensen, K. F.; Bawendi, M. G. (CdSe)ZnS Core-Shell Quantum Dots: Synthesis and Characterization of a Size Series of Highly Luminescent Nanocrystallites. *The Journal of Physical Chemistry B* **Nov. 1997**, *101*, 9463–9475.

(64) Peng, X.; Schlamp, M. C.; Kadavanich, A. V.; Alivisatos, A. P. Epitaxial growth of highly luminescent CdSe/CdS core/shell nanocrystals with photostability and electronic accessibility. *Journal of the American Chemical Society* **1997**, *119*, 7019–7029.

(65) Swabeck, J. K.; Fischer, S.; Bronstein, N. D.; Alivisatos, A. P. Broadband Sensitization of Lanthanide Emission with Indium Phosphide Quantum Dots for Visible to Near-Infrared Downshifting. *Journal of the American Chemical Society* **July 2018**, *140*, 9120–9126.

(66) Xie, R.; Battaglia, D.; Peng, X. Colloidal InP Nanocrystals as Efficient Emitters Covering Blue to Near-Infrared. *Journal of the American Chemical Society* **Dec. 2007**, *129*, 15432–15433.

(67) Reiss, P.; Protière, M.; Li, L. Core/shell semiconductor nanocrystals. *Small* **2009**, *5*, 154–168.

(68) Lim, J.; Bae, W. K.; Lee, D.; Nam, M. K.; Jung, J.; Lee, C.; Char, K.; Lee, S. InP@ZnSeS, Core@Composition Gradient Shell Quantum Dots with Enhanced Stability. *Chemistry of Materials* **Oct. 2011**, *23*, 4459–4463.

(69) Talapin, D. V.; Nelson, J. H.; Shevchenko, E. V.; Aloni, S.; Sadtler, B.; Alivisatos, A. P. Seeded Growth of Highly Luminescent CdSe/CdS Nanoheterostructures with Rod and Tetrapod Morphologies. *Nano Letters* **Oct. 2007**, *7*, 2951–2959.

(70) Sun, S.; Yuan, D.; Xu, Y.; Wang, A.; Deng, Z. Ligand-Mediated Synthesis of Shape-Controlled Cesium Lead Halide Perovskite Nanocrystals via Reprecipitation Process at Room Temperature. *ACS Nano* **Mar. 2016**, *10*, 3648–3657.

(71) Macfarlane, R. J.; Lee, B.; Jones, M. R.; Harris, N.; Schatz, G. C.; Mirkin, C. A. Nanoparticle Superlattice Engineering with DNA. *Science* **Oct. 2011**, *334*, 204–208.

(72) Yang, Y.; Qin, H.; Jiang, M.; Lin, L.; Fu, T.; Dai, X.; Zhang, Z.; Niu, Y.; Cao, H.; Jin, Y.; Zhao, F.; Peng, X. Entropic Ligands for Nanocrystals: From Unexpected Solution Properties to Outstanding Processability. **2016**, 6–11.

(73) Koscher, B. A.; Swabeck, J. K.; Bronstein, N. D.; Alivisatos, A. P. Essentially Trap-Free $CsPbBr_3$ Colloidal Nanocrystals by Postsynthetic Thiocyanate Surface Treatment. *Journal of the American Chemical Society* **May 2017**, *139*, 6566–6569.

(74) Nenon, D. P.; Pressler, K.; Kang, J.; Koscher, B. A.; Olshansky, J. H.; Osowiecki, W. T.; Koc, M. A.; Wang, L.-W.; Alivisatos, A. P. Design Principles for Trap-Free $CsPbX_3$ Nanocrystals: Enumerating and Eliminating Surface Halide Vacancies with Softer Lewis Bases. *Journal of the American Chemical Society* **Dec. 2018**, *140*, 17760–17772.

(75) Talapin, D. V.; Gaponik, N.; Borchert, H.; Rogach, A. L.; Haase, M.; Weller, H. Etching of colloidal InP nanocrystals with fluorides: Photochemical nature of the process resulting in high photoluminescence efficiency. *Journal of Physical Chemistry B* **2002**, *106*, 12659–12663.

(76) Adam, S.; McGinley, C.; Möller, T.; Talapin, D. V.; Borchert, H.; Haase, M.; Weller, H. Photoemission study of size selected InP nanocrystals: the relationship between luminescence yield and surface structure. *The European Physical Journal D - Atomic, Molecular and Optical Physics* **June 2003**, *24*, 373–376.

(77) Adam, S.; Talapin, D. V.; Borchert, H.; Lobo, A.; Mcginley, C.; Castro, A. R. B. D.; Haase, M.; Weller, H.; Adam, S. The effect of nanocrystal surface structure on the luminescence properties : Photoemission study of HF-etched InP nanocrystals. *The Journal of Chemical Physics* **2005**, *123*, DOI: 10.1063/1.2004901.

(78) Goldschmidt, J. C.; Fischer, S. Upconversion for photovoltaics - a review of materials, devices and concepts for performance enhancement. *Advanced Optical Materials* **2015**, *3*, 510–535.

(79) Huang, X.; Han, S.; Huang, W.; Liu, X. Enhancing solar cell efficiency: the search for luminescent materials as spectral converters. *Chem. Soc. Rev.* **2013**, *42*, 173–201.

(80) Correia, S. F. H.; de Zea Bermudez, V.; Ribeiro, S. J. L.; André, P. S.; Ferreira, R. A. S.; Carlos, L. D. Luminescent solar concentrators: challenges for lanthanide-based organic-inorganic hybrid materials. *J. Mater. Chem. A* **2014**, *2*, 5580–5596.

(81) Wang, F.; Banerjee, D.; Liu, Y.; Chen, X.; Liu, X. Upconversion nanoparticles in biological labeling, imaging, and therapy. *The Analyst* **2010**, *135*, 1839.

(82) Vetrone, F.; Naccache, R.; Zamarroǹ, A.; Juarranz de la Fuente, A.; Sanz-Rodrígguez, F.; Martinez Maestro, L.; Martiǹ Rodriguez, E.; Jaque, D.; Garcià Solè, J.; Capobianco, J. A. Temperature Sensing Using Fluorescent Nanothermometers. *ACS Nano* **2010**, *4*, 3254–3258.

(83) Bettinelli, M.; Carlos, L.; Liu, X. Lanthanide-doped upconversion nanoparticles. *Physics Today* **2015**, *68*, 38–44.

(84) Auzel, F. Upconversion and Anti-Stokes Processes with f and d Ions in Solids. *Chemical Reviews* **2004**, *104*, 139–173.

(85) Wang, X.; Valiev, R. R.; Ohulchanskyy, T. Y.; Ågren, H.; Yang, C.; Chen, G. Dye-sensitized lanthanide-doped upconversion nanoparticles. *Chem. Soc. Rev.* **2017**, *46*, 4150–4167.

(86) Moore, E. G.; Samuel, A. P. S.; Raymond, K. N. From antenna to assay: lessons learned in lanthanide luminescence. *Accounts of Chemical Research* **2009**, *42*, 542–552.

(87) Hu, J.-Y.; Ning, Y.; Meng, Y.-S.; Zhang, J.; Wu, Z.-Y.; Gao, S.; Zhang, J.-L. Highly near-IR emissive ytterbium(iii) complexes with unprecedented quantum yields. *Chem. Sci.* **2017**, *8*, 2702–2709.

(88) Beeby, A.; Clarkson, I. M.; Dickins, R. S.; Faulkner, S.; Parker, D.; Royle, L.; de Sousa, A. S.; Williams, J. A. G.; Woods, M. Non-radiative deactivation of the excited states of europium, terbium and ytterbium complexes by proximate energy-matched OH, NH and CH oscillators: an improved luminescence method for establishing solution hydration states. *Journal of the Chemical Society, Perkin Transactions 2* **1999**, *2*, 493–504.

(89) Chen, D.; Wang, Y.; Yu, Y.; Huang, P.; Weng, F. Quantum cutting downconversion by cooperative energy transfer from Ce^{3+} to Yb^{3+} in borate glasses. *Journal of Applied Physics* **2008**, *104*, 1–4.

(90) Stephan, M.; Zachau, M.; Gröting, M.; Karplak, O.; Eyert, V.; Mishra, K.; Schmidt, P. A theoretical investigation of 4f-5d transition of trivalent rare earth ions in fluorides and complex oxides. *Journal of Luminescence* **Sept. 2005**, *114*, 255–266.

(91) Creutz, S. E.; Fainblat, R.; Kim, Y.; De Siena, M. C.; Gamelin, D. R. A Selective Cation Exchange Strategy for the Synthesis of Colloidal Yb^{3+}-Doped Chalcogenide Nanocrystals with Strong Broadband Visible Absorption and Long-Lived Near-Infrared Emission. *Journal of the American Chemical Society* **2017**, *139*, 11814–11824.

(92) Milstein, T. J.; Kroupa, D. M.; Gamelin, D. R. Picosecond Quantum Cutting Generates Photoluminescence Quantum Yields Over 100% in Ytterbium-Doped $CsPbCl_3$ Nanocrystals. *Nano Letters* **May 2018**, acs.nanolett.8b01066.

(93) Ribeiro, C. T. M.; Zanatta, A. R.; Nunes, L. A. O.; Messaddeq, Y.; Aegerter, M. A. Optical spectroscopy of Er^{3+} and Yb^{3+} co-doped fluoroindate glasses. *Journal of Applied Physics* **1998**, *83*, 2256–2260.

(94) Alivisatos, A. P. Semiconductor Clusters, Nanocrystals, and Quantum Dots. *Science* **Feb. 1996**, *271*, 933–937.

(95) Martín-Rodríguez, R.; Geitenbeek, R.; Meijerink, A. Incorporation and luminescence of Yb^{3+} in CdSe nanocrystals. *Journal of the American Chemical Society* **2013**, *135*, 13668–13671.

(96) Kushida, T.; Geusic, J. E. Optical Refrigeration in Nd-Doped Yttrium Aluminum Garnet. *Phys. Rev. Lett.* **Oct. 1968**, *21*, 1172–1175.

(97) Fischer, S.; Swabeck, J. K.; Alivisatos, A. P. Controlled Isotropic and Anisotropic Shell Growth in β-NaLnF4 Nanocrystals Induced by Precursor Injection Rate. *Journal of the American Chemical Society* **2017**, *139*, 12325–12332.

(98) Ye, X.; Chen, J.; Engel, M.; Millan, J. A.; Li, W.; Qi, L.; Xing, G.; Collins, J. E.; Kagan, C. R.; Li, J.; Glotzer, S. C.; Murray, C. B. Competition of shape and interaction patchiness for self-assembling nanoplates. *Nature Chemistry* **May 2013**, *5*, 466–473.

(99) Tamang, S.; Lincheneau, C.; Hermans, Y.; Jeong, S.; Reiss, P. Chemistry of InP Nanocrystal Syntheses. *Chemistry of Materials* **Apr. 2016**, *28*, 2491–2506.

(100) Taguchi, A.; Takahei, K.; Horikoshi, Y. Multiphonon-assisted energy transfer between Yb 4f shell and InP host. *Journal of Applied Physics* **1994**, *76*, 7288.

(101) Watts, R. K.; Richter, H. J. Diffusion and transfer of optical excitation in YF_3: Yb, Ho. *Physical Review B* **1972**, *6*, 1584–1589.

(102) Hudry, D.; Busko, D.; Popescu, R.; Gerthsen, D.; Abeykoon, A. M. M.; Kübel, C.; Bergfeldt, T.; Richards, B. S. Direct Evidence of Significant Cation Intermixing in Upconverting Core@Shell Nanocrystals: Toward a New Crystallochemical Model. *Chemistry of Materials* **Nov. 2017**, *29*, 9238–9246.

(103) Fischer, S.; Martín-Rodríguez, R.; Fröhlich, B.; Krämer, K. W.; Meijerink, A.; Goldschmidt, J. C. Upconversion quantum yield of Er^{3+}-doped β-$NaYF_4$ and Gd_2O_2S: The effects of host lattice, Er^{3+} doping, and excitation spectrum bandwidth. *Journal of Luminescence* **Sept. 2014**, *153*, 281–287.

(104) Resch-Genger, U.; Grabolle, M.; Cavaliere-Jaricot, S.; Nitschke, R.; Nann, T. Quantum dots versus organic dyes as fluorescent labels. *Nature Methods* **Sept. 2008**, *5*, 763–775.

(105) Hanifi, D. A.; Bronstein, N. D.; Koscher, B. A.; Nett, Z.; Swabeck, J. K.; Takano, K.; Schwartzberg, A. M.; Maserati, L.; Vandewal, K.; van de Burgt, Y.; Salleo, A.; Alivisatos, A. P. Redefining near-unity luminescence in quantum dots with photothermal threshold quantum yield. *Science* **Mar. 2019**, *363*, 1199–1202.

(106) Kagan, C. R.; Lifshitz, E.; Sargent, E. H.; Talapin, D. V. Building devices from colloidal quantum dots. *Science* **Aug. 2016**, *353*, aac5523–aac5523.

(107) Dai, X.; Zhang, Z.; Jin, Y.; Niu, Y.; Cao, H.; Liang, X.; Chen, L.; Wang, J.; Peng, X. Solution-processed, high-performance light-emitting diodes based on quantum dots. *Nature* **Nov. 2014**, *515*, 96–99.

(108) Akkerman, Q. A.; D'Innocenzo, V.; Accornero, S.; Scarpellini, A.; Petrozza, A.; Prato, M.; Manna, L. Tuning the Optical Properties of Cesium Lead Halide Perovskite Nanocrystals by Anion Exchange Reactions. *Journal of the American Chemical Society* **Aug. 2015**, *137*, 10276–10281.

(109) Nedelcu, G.; Protesescu, L.; Yakunin, S.; Bodnarchuk, M. I.; Grotevent, M. J.; Kovalenko, M. V. Fast Anion-Exchange in Highly Luminescent Nanocrystals of Cesium Lead Halide Perovskites ($CsPbX_3$, X = Cl, Br, I). *Nano Letters* **Aug. 2015**, *15*, 5635–5640.

(110) Raja, S. N.; Bekenstein, Y.; Koc, M. A.; Fischer, S.; Zhang, D.; Lin, L.; Ritchie, R. O.; Yang, P.; Alivisatos, A. P. Encapsulation of Perovskite Nanocrystals into Macroscale Polymer Matrices: Enhanced Stability and Polarization. *ACS Applied Materials & Interfaces* **Dec. 2016**, *8*, 35523–35533.

(111) Cui, J.; Beyler, A. P.; Marshall, L. F.; Chen, O.; Harris, D. K.; Wanger, D. D.; Brokmann, X.; Bawendi, M. G. Direct probe of spectral inhomogeneity reveals synthetic tunability of single-nanocrystal spectral linewidths. *Nature Chemistry* **July 2013**, *5*, 602–606.

(112) Giansante, C.; Infante, I. Surface Traps in Colloidal Quantum Dots: A Combined Experimental and Theoretical Perspective. *The Journal of Physical Chemistry Letters* **Oct. 2017**, *8*, 5209–5215.

(113) Bullen, C.; Mulvaney, P. The effects of chemisorption on the luminescence of CdSe quantum dots. *Langmuir* **2006**, *22*, 3007–3013.

(114) Ghai, R.; Falconer, R. J.; Collins, B. M. Applications of isothermal titration calorimetry in pure and applied research-survey of the literature from 2010. *Journal of Molecular Recognition* **2012**, *25*, 32–52.

(115) Lin, W.; Walter, J.; Burger, A.; Maid, H.; Hirsch, A.; Peukert, W.; Segets, D. A General Approach To Study the Thermodynamics of Ligand Adsorption to Colloidal Surfaces Demonstrated by Means of Catechols Binding to Zinc Oxide Quantum Dots. *Chemistry of Materials* **2015**, *27*, 358–369.

(116) Jharimune, S.; Sathe, A. A.; Rioux, R. M. Thermochemical Measurements of Cation Exchange in CdSe Nanocrystals Using Isothermal Titration Calorimetry. *Nano Letters* **2018**, *18*, 6795–6803.

(117) Yang, B.; Liu, R.; Hao, X.; Wu, Y.; Du, J. Effect of CdTe Quantum Dots Size on the Conformational Changes of Human Serum Albumin: Results of Spectroscopy and Isothermal Titration Calorimetry. *Biological Trace Element Research* **Oct. 2013**, *155*, 150–158.

(118) Shen, Y.; Tan, R.; Gee, M. Y.; Greytak, A. B. Quantum Yield Regeneration: Influence of Neutral Ligand Binding on Photophysical Properties in Colloidal Core/Shell Quantum Dots. *ACS Nano* **2015**, *9*, 3345–3359.

(119) Gourishankar, A.; Shukla, S.; Ganesh, K. N.; Sastry, M. Isothermal Titration Calorimetry Studies on the Binding of DNA Bases and PNA Base Monomers to Gold Nanoparticles. *Journal of the American Chemical Society* **2004**, *126*, 13186–13187.

(120) Gomes, R.; Hassinen, A.; Szczygiel, A.; Zhao, Q.; Vantomme, A.; Martins, J. C.; Hens, Z. Binding of phosphonic acids to CdSe quantum dots: A solution NMR study. *Journal of Physical Chemistry Letters* **2011**, *2*, 145–152.

(121) Dubois, F.; Mahler, B.; Dubertret, B.; Doris, E.; Mioskowski, C. A Versatile Strategy for Quantum Dot Ligand Exchange. *Journal of the American Chemical Society* **2007**, *129*, 482–483.

(122) Cros-Gagneux, A.; Delpech, F.; Nayral, C.; Cornejo, A.; Coppel, Y.; Chaudret, B. Surface Chemistry of InP Quantum Dots: A Comprehensive Study. *Journal of the American Chemical Society* **2010**, *132*, 18147–18157.

(123) Hens, Z.; Martins, J. C. A solution NMR toolbox for characterizing the surface chemistry of colloidal nanocrystals. *Chemistry of Materials* **2013**, *25*, 1211–1221.

(124) Hassinen, A.; Moreels, I.; De Nolf, K.; Smet, P. F.; Martins, J. C.; Hens, Z. Short-chain alcohols strip X-type ligands and quench the luminescence of PbSe and CdSe quantum Dots, acetonitrile does not. *Journal of the American Chemical Society* **2012**, *134*, 20705–20712.

(125) Ravel, B.; Newville, M. ATHENA , ARTEMIS , HEPHAESTUS : data analysis for X-ray absorption spectroscopy using IFEFFIT. *Journal of Synchrotron Radiation* **July 2005**, *12*, 537–541.

(126) Bronstein, N. D.; Yao, Y.; Xu, L.; O'Brien, E.; Powers, A. S.; Ferry, V. E.; Alivisatos, A. P.; Nuzzo, R. G. Quantum Dot Luminescent Concentrator Cavity Exhibiting 30-fold Concentration. *ACS Photonics* **Nov. 2015**, *2*, 1576–1583.